Fast Computation of Terrain-Induced Gravitational and Magnetic Effects on Arbitrary Undulating Surfaces

Leyuan Wu[1] · Longwei Chen[2]

Abstract

Based on a brief review of forward algorithms for the computation of topographic gravitational and magnetic effects, including spatial, spectral and hybrid-domain algorithms working in either Cartesian or spherical coordinate systems, we introduce a new algorithm, namely the CP-FFT algorithm, for fast computation of terrain-induced gravitational and magnetic effects on arbitrary undulating surfaces. The CP-FFT algorithm, working in the hybrid spatial-spectral domain, is based on a combination of CANDECOMP/PARAFAC (CP) tensor decomposition of gravitational integral kernels and 2D Fast Fourier Transform (FFT) evaluation of discrete convolutions. By replacing the binomial expansion in classical FFT-based terrain correction algorithms using CP decomposition, convergence of the outer-zone computation can be achieved with significantly reduced inner-zone radius. Additionally, a Gaussian quadrature mass line model is introduced to accelerate the computation of the inner zone effect. We validate our algorithm by computing the gravitational potential, the gravitational vector, the gravity gradient tensor, and magnetic fields caused by densely-sampled topographic and bathymetric digital elevation models of selected mountainous areas around the globe. Both constant and variable density/magnetization models, with computation surfaces on, above and below the topography are considered. Comparisons between our new method and space-domain rigorous solutions show that with modeling errors well below existing instrumentation error levels, the calculation speed is accelerated thousands of times in all numerical tests. We release a set of open-source code written in MATLAB language to meet the needs of geodesists and geophysicists in related fields to carry out more efficiently topographic modeling in Cartesian coordinates under planar approximation.

✉ Longwei Chen
  longweichen_glut@glut.edu.cn

Extended author information available on the last page of the article

Article Highlights

- A new algorithm is presented for the efficient computation of terrain-induced gravitational and magnetic fields on arbitrary surfaces
- Tensor decomposition instead of the classical binomial expansion is used to achieve optimal approximations of the integral kernel functions
- The new method is validated by comparing with space-domain rigorous solutions using various densely-sampled digital elevation models

1 Introduction

The calculation of the gravitational potential (GP), the gravitational vector (GV), the gravity gradient tensor (GGT), and magnetic fields on a surface describing the measurement positions from varying terrain with constant or variable density/magnetization is a classical problem in geophysics and geodesy (Pedersen et al. 2015). In geophysical study, for ground-based, airborne or near-seabed measurements, observations are made on an undulating surface above the local topography or bathymetry. Therefore, it is desirable to remove terrain-induced gravitational and magnetic effects from observed data in order to isolate the anomalies to be investigated (Plouff 1976; Grauch 1987; Hildenbrand et al. 1993; Bouligand et al. 2014), or to interpret the anomalous sources that contain the terrain as a whole (Parker and Huestis 1974; Macdonald et al. 1983; Tontini et al. 2008; Searle et al. 2019). In both cases, an efficient algorithm for computing topographic gravitational and magnetic effects on arbitrary undulating surfaces plays a central role.

In geodesy, topographic global gravity field models of the Earth (Grombein et al. 2016; Rexer et al. 2016; Ince et al. 2020), obtained by forward calculation of the gravity effect caused by some global topographic models, such as the 1 arc-sec resolution Earth2014 model (Hirt and Rexer 2015), are organized and updated at the International Centre for Global Earth Models (ICGEM) (Ince et al. 2019). They are useful in spectral augmentation of global gravity models based on satellite and terrestrial gravity measurements (Hirt et al. 2013; Rexer 2017; Zingerle et al. 2020; Ince et al. 2020), in filling the gaps where actual gravity observations are limited or unavailable (Pavlis et al. 2012), and also in deriving global Bouguer and isostatic gravity anomaly maps (Balmino et al. 2012).

Generally speaking, there are three major algorithms for computing terrain-induced gravitational and magnetic fields, including space-domain (or spatial-domain) algorithms, spectral-domain algorithms (sometimes called Fourier-domain algorithms in local studies under planar approximation), and hybrid space-spectral domain algorithms. Each of them can be further subdivided into several different types according to the specific forward computation required in either local, regional or global modeling.

Space-domain algorithms are based on the superposition principle of gravitational and magnetic fields. Usually the topographic source is decomposed into a bunch of mass elements, including polyhedron (Werner and Scheeres 1997; Holstein 2003; Jekeli and Zhu 2006; Tsoulis 2012; D'Urso and Trotta 2017; Ren et al. 2018; Zhang and Chen 2018; Holzrichter et al. 2019; Saraswati et al. 2019), rectangular prism (Bhattacharyya 1964; Nagy et al. 2000; Garcia-Abdeslem 2005; Jiang et al. 2018; Karcol 2018; Fukushima 2020), spherical/spheroidal/ellipsoidal prism (tesseroid) (Asgharzadeh et al. 2007; Du et al. 2015; Roussel et al. 2015; Baykiev et al. 2016; Grombein et al. 2016; Uieda et al. 2016; Deng and Shen 2018; Fukushima 2018; Lin et al. 2020), mass line and mass point (Heck and Seitz 2007; Wild-Pfeiffer 2008), and the

contributions for each element are calculated and summed together. Depending on the attenuation character of Newton's integral kernel with distance, it is numerically more advantageous to use a combination of multiple mass elements for forward simulation than to use a single one. Simpler mass elements, such as the mass line and mass point, accompanied usually by DEMs with reduced spatial resolution, can be applied for far-zone effect computation to accelerate the forward process. More complex elements, such as the polyhedron and the rectangular prism, accompanied by high-resolution DEMs, provide more accurate near-zone effect which are critical to maintain the high frequency part of the true results (Tsoulis et al. 2009; Cella 2015; Benedek et al. 2018; Hirt et al. 2019; Yang et al. 2020). Although GPU and parallel programming techniques can be applied to improve the speed of computation (Moorkamp et al. 2010; Zhang et al. 2015), space-domain algorithms are still computationally expensive for forward modeling over large areas using detailed DEMs.

Spectral-domain algorithms refer to Fast Fourier Transform (FFT) based algorithms for local terrain modeling in Cartesian coordinate system, and spherical harmonic transform (SHT) based algorithms for global modeling in spherical coordinate system. The former, to which this work is closely related, shall be discussed later. The latter, when applied for the modeling of gravitational and magnetic fields on a sphere (with constant radius) due to finite amplitude topography, can be understood as the spherical analog to the Cartesian result of Parker (1973). This algorithm and its extensions have been extensively used in calculating topographic gravitational field models caused by terrestrial planets (Rummel et al. 1988; Martinec et al. 1989; Balmino 1994; Wieczorek and Phillips 1998; Ramillien 2002; Featherstone et al. 2013; Hirt and Kuhn 2014; Tenzer et al. 2015; Wieczorek 2015; Sprlak et al. 2018; Ince et al. 2020). By combining with upward and downward continuation techniques, the algorithm can also be extended to the computation of gravitational fields on the rugged surfaces of planetary bodies (Balmino et al. 2012; Hirt 2012; Bucha and Janák 2014; Rexer et al. 2016; Bucha et al. 2019b).

Despite its popularity in topographic potential modeling, it has been proved mathematically that regardless of the smoothness of the density and topography, spherical harmonic series converges exactly in the closure of the exterior of the Brillouin sphere, and convergence below the Brillouin sphere occurs with probability zero (Costin et al. 2022). A great many recent numerical experiments also support this conclusion (Hirt and Kuhn 2017; Bucha and Sansò 2021; Sprlak and Han 2021). Divergence of the series occurs at higher degrees for large-sized, near-spherical planets such as the Earth and the Moon, but may occur at much lower degrees for medium and small-sized, non-spherical, irregularly shaped asteroids, comets and moons (Hu and Jekeli 2015; Reimond and Baur 2016; Bucha and Sansò 2021). Convergence behavior can be improved, especially for computation points lie between the Brillouin sphere and the Brillouin spheroid/ellipsoid, by applying spheroidal/ellipsoidal harmonic series instead (Garmier et al. 2002; Claessens and Hirt 2013; Wang and Yang 2013; Rexer et al. 2016; Sprlak et al. 2020). However, this does not fundamentally change the divergent nature of the series. Alternatively, a combination of external/internal spherical harmonic series expansions may be a feasible scheme (Górski et al. 2018; Bucha and Sansò 2021; Sprlak and Han 2021), but still adds lots of additional computation spheres, each with a different set of harmonic coefficients, and extra interpolation when forward results are required on an arbitrary undulating surface.

Hybrid space-spectral domain algorithms, compared with the previous two, have better performance in balancing the contradiction between numerical accuracy and efficiency. They rely on a combination of FFT/SHT and space-domain rigorous formula in solving local/global terrain modeling problems, respectively. The FFT-based hybrid algorithm, to which this work belongs, shall be discussed in detail later. To implement the SHT-based hybrid algorithm for global terrain modeling, as far as we know, there are two approaches.

One is to decompose the topography using the residual terrain modeling (RTM) technique (Hirt et al. 2019), the other is to modify Newton's integral kernel within a certain spherical distance (Bucha et al. 2019a; Bucha and Kuhn 2020). The essential idea of both two methods is to decompose the target forward field into two parts, one of which contains only low frequency (long-wavelength) constituents. Since gravitational computation can be expressed as the convolution of the DEM and Newton's integral kernel, this can be done either by using a low-pass filtered DEM (e.g., the RTM technique) (Hirt et al. 2019), or a modified band-limited convolution kernel (Bucha et al. 2019a). In this way, divergence of the spherical harmonic series can be controlled within acceptable limits even at the planet's surface. The residual terrain, or the near-zone effects, which contain extremely rich high-frequency components, are evaluated rigorously by some space-domain solutions, such as the polyhedron or the rectangular prism. Since the space-domain evaluation is required only within a certain spherical distance for each computation point, the speed advantage of spectral domain method can be well preserved. Reported values for the space-domain integration radius are about 15 km for the Moon (Bucha and Kuhn 2020), and 40 km for the Earth (Hirt et al. 2019), these may be sufficient for global modeling using low-resolution DEMs, but are still computationally too expensive for local terrain modeling with high-resolution DEMs.

FFT-based algorithms, to which this work belongs, are suitable for topographic modeling in Cartesian coordinates under planar approximation. To our knowledge, there are four types of FFT-based algorithms applicable for the computation of terrain-induced gravity or magnetic fields on an undulating surface. Two of them based on 2D FFT, and the other two on 3D FFT, depending on whether the analytical or the discrete kernel spectrum is used (Sanso and Sideris 2013, page 462):

1. The first 2D FFT algorithm is a simple extension of Parker's method using the analytical kernel spectrum (Parker 1973). By combining forward modeling on a horizontal plane above the topography and downward continuation using Taylor series expansion, forward results on a draped surface can be calculated efficiently (Pedersen et al. 2015; Wu 2021). However, in this way only a low-pass filtered version of the true terrain effect can be obtained due to the unstable downward continuation process.

2. The second 2D FFT algorithm, which is based on the discrete kernel spectrum and binomial expansion (Forsberg 1984, 1985), is more popular in geodetic studies for computing gravimetric terrain corrections. FFT here no longer serves as the numerical counterpart (rectangle or trapezoidal quadrature rule) of the continuous Fourier transform, but as a tool for the accurate evaluation of Toeplitz matrix–vector multiplications after embedding into a circulant matrix–vector multiplication system (Wu 2018). Despite that this algorithm has been studied and improved by many authors, it still requires a large part of space-domain computation to ensure convergence of the spectral part due to the limitation of using binomial expansions (Sideris 1984; Li and Sideris 1994; Martinec et al. 1996; Parker 1996; Tsoulis 2001; Goyal et al. 2020).

3. Analogously, the first 3D FFT algorithm is to use the 3D analytical spectrum of the Newton's kernel (Tontini et al. 2009). The topographic source is first decomposed into a 3D grid of rectangular prisms, after which 3D FFTs are applied to calculate gravity or magnetic fields also on a 3D regular grid. Forward values on arbitrary surfaces can be obtained through interpolation. The method suffers from spectral leakage and truncation errors (Wu and Tian 2014). Improved version of the algorithm is introduced in Zhao et al. (2018) based on the Gauss-FFT algorithm (Wu 2016).

4. The second 3D FFT algorithm, which is based on the discrete kernel spectrum, applies 3D FFTs to evaluate 3D discrete convolutions (Sanso and Sideris 2013, page 468, 473). The zero-padding technique applied to eliminate edge effects is in fact mathematically equivalent to the Toeplitz-circulant matrix embedding process (Zhang and Wong 2015; Wu 2018; Chen and Liu 2019; Hogue et al. 2020; Vatankhah et al. 2022). The advantage of using a 3D FFT algorithm is that 3D variable density or magnetization can be incorporated easily. However, since regular 3D grids are used both in decomposing the topographic source and in defining computation coordinates, and topographic or observation height values are somehow arbitrary, usually it requires a very small grid step in the vertical direction (e.g., 5 m or even less) to guarantee the modeling accuracy at the expense of increased storage and computational efforts.

In this study, we introduce a CP-FFT algorithm, a new hybrid spatial-spectral domain algorithm working in Cartesian coordinates, for fast and accurate computation of terrain-induced gravitational and magnetic effects on arbitrary undulating surfaces. We start by analyzing the key idea of the classical FFT-based terrain correction algorithm, based on which we make a significant step by embedding the CP tensor decomposition into the approximation of the terrain correction convolution kernel. Next we extend our new method to all gravitational components commonly applied, and to magnetic field modeling through the Poisson's relation. Finally, we test our algorithm using topographic and bathymetric datasets around the globe by comparing to space-domain rigorous solutions. We release a set of open source codes written in MATLAB language to scientists working in a related field.

2 Algorithm Formulations

2.1 The Classical Terrain Correction Algorithm

We denote $r = (x, y, z)$ as the computation point, $\tilde{r} = (\tilde{x}, \tilde{y}, \tilde{z})$ as the running integration point, and $R = |r - \tilde{r}|$ is the Euclidean distance between the computation and the integration point. The coordinate system is chosen with positive x pointing north, positive y pointing east, and positive z pointing downward. Suppose we have the topographic height function $\tilde{z} = h(\tilde{x}, \tilde{y})$, the computation required on an undulating surface $z = H(x, y)$, the integration is carried out over the rectangular area $\Omega = [X1, X2] \times [Y1, Y2]$, with topographic masses outside this region ignored, then the gravitational terrain correction can be written as (Goyal et al. 2020):

$$
\begin{aligned}
g_z^{tc}(x, y, H) &= G\rho \int_{Y1}^{Y2} \int_{X1}^{X2} \int_{H}^{h} \frac{\partial}{\partial z}\left(\frac{1}{R}\right) d\tilde{x}d\tilde{y}d\tilde{z} \\
&= G\rho \int_{Y1}^{Y2} \int_{X1}^{X2} \left(\frac{1}{L}\left[1 - \left(1 + \left(\frac{H-h}{L}\right)^2\right)^{-\frac{1}{2}}\right]\right) d\tilde{x}d\tilde{y},
\end{aligned} \tag{1}
$$

where G is Newton's gravitational constant, ρ is the constant topographic density, and $L = \sqrt{(x - \tilde{x})^2 + (y - \tilde{y})^2}$ is the planar Euclidean distance.

By expanding the term $\left[1 + \left(\frac{H-h}{L}\right)^2\right]^{-\frac{1}{2}}$ into a binomial series according to

$$(1 + x)^{-\frac{1}{2}} \approx \sum_{n=0}^{N_B} (-1)^n \frac{(2n-1)!!}{(2n)!!} x^n = 1 - \frac{1}{2}x + \frac{1 \cdot 3}{2 \cdot 4}x^2 - \frac{1 \cdot 3 \cdot 5}{2 \cdot 4 \cdot 6}x^3 + \cdots, \quad (2)$$

with N_B the order of expansion, we have:

$$g_z^{tc}(x, y, H) \approx G\rho \int_{Y1}^{Y2} \int_{X1}^{X2} \left[\frac{(H-h)^2}{2L^3} - \frac{3(H-h)^4}{8L^5} + \frac{15(H-h)^6}{48L^7} - \cdots \right] d\tilde{x}d\tilde{y}, \quad (3)$$

in which the variables L, H and h can be separated, recasting the expression into a weighted summation of a series of continuous convolutions:

$$g_z^{tc}(x, y, H) \approx G\rho \sum_{(i_1, i_2, i_3)} \omega_{(i_1, i_2, i_3)} H^{i_1} \left(h^{i_2} * L^{-i_3} \right), \quad (4)$$

with (i_1, i_2, i_3) representing all combinations of integer powers of H, h and L after Eq. 3 is full expanded, $\omega_{(i_1, i_2, i_3)}$ the corresponding coefficients, and the symbol $*$ indicating continuous convolutions of two functions.

After discretizing the integration region Ω using a regular grid of mass line or mass prism elements, the continuous convolution-type integrals reduce to discrete convolutions (Li and Sideris 1994), which can then be evaluated accurately and efficiently by combining circulant embedding of Toeplitz matrix–vector multiplications with FFT-based algorithms (Vogel 2002; Zhang and Wong 2015; Wu 2018; Chen and Liu 2019).

Although this binomial expansion method works perfectly well for a mildly varying topography, it has been clearly demonstrated in many previous works that its convergence depends strictly on the condition $\left| \frac{H-h}{L} \right| \leq 1$ (Tsoulis 2001; Goyal et al. 2020), meaning that the slope of every line connecting a computation point and an integration point should not exceed 45°, which is a strong restriction that can be easily violated by steeply varying topographic models in most mountainous areas of the Earth.

Denoting the integral kernel function in Eq. 1 as:

$$\mathcal{K}_{g_z}^{tc}(L, H, h) = \frac{1}{L} - \frac{1}{\sqrt{L^2 + (H-h)^2}}, \quad (5)$$

the divergence problem has been partially solved by using a separating radius R_{FFT} to divide the terrain correction integration into two zones (Tsoulis 2001; Goyal et al. 2020):

$$\begin{aligned} g_z^{tc}(x, y, H) &= \hat{g}_z^{tc}(x, y, H) + \bar{g}_z^{tc}(x, y, H) \\ &= G\rho \iint_{L < R_{FFT}} \mathcal{K}_{g_z}^{tc} d\tilde{x}d\tilde{y} + G\rho \iint_{L \geq R_{FFT}} \mathcal{K}_{g_z}^{tc} d\tilde{x}d\tilde{y}, \end{aligned} \quad (6)$$

with the inner zone effect $\hat{g}_z^{tc}$ computed using space-domain rigorous solutions, and the outer zone effect $\bar{g}_z^{tc}$ evaluated using the FFT-based procedure described above. However, there remain unresolved issues with this combined approach: (1) to ensure convergence, usually a large radius R_{FFT} is required, leading to time-consuming evaluation of the inner zone effect using space-domain solutions; (2) the algorithm is designed only for the g_z component, whether it can be effectively extended to the forward modeling of other GP, GV, GGT components and magnetic fields still needs further investigations. These problems become particularly prominent when various gravitational and magnetic components

are required from large-scale, high-resolution topographic or bathymetric models. In the following, we introduce a new CP-FFT method to overcome these deficiencies.

2.2 Improved Terrain Correction Algorithm Using CP Tensor Decomposition

The key idea behind terrain correction computation is the approximation of the integral kernel $\mathcal{K}_{g_z}^{tc}(L, H, h)$ using a summation of products of single-variable functions $A(L)$, $B(H)$ and $C(h)$. Taylor series expansions (including the binomial expansion), even with optimally chosen parameters (Li and Sideris 1994), have been proved invalid in mountainous areas when densely-sampled DEMs (e.g., < 100 m resolution) are used (Tsoulis 2001; Goyal et al. 2020). Combining space-domain solution to evaluate a circular region surrounding each computation point with a large radius (R_{FFT}) will slow down the entire process significantly. Here we introduce an alternative approach based on CANDECOMP/PARAFAC (CP) tensor decomposition of the terrain correction kernel function.

As shown in Fig. 1a, first the 3D kernel function $\mathcal{K}_{g_z}^{tc}(L, H, h)$ is sampled on a rectilinear grid covering the region of interest:

$$(L, H, h) \in [L_{\min}, L_{\max}] \times [H_{\min}, H_{\max}] \times [h_{\min}, h_{\max}], \tag{7}$$

with:

$$
\begin{aligned}
L_i &= L_{min} s^{i-1}, \quad i = 1, 2, \cdots, N_L, \\
H_j &= H_{min} + (j-1)\Delta H, \quad j = 1, 2, \cdots, N_H, \\
h_k &= h_{min} + (k-1)\Delta h, \quad k = 1, 2, \cdots, N_h,
\end{aligned} \tag{8}
$$

whereas $s = \frac{L_{\max}}{L_{\min}}^{\frac{1}{N_L - 1}}$ is the common ratio of the geometric sequence L_i, and $\Delta H = \frac{H_{\max} - H_{\min}}{N_H - 1}$, $\Delta h = \frac{h_{\max} - h_{\min}}{N_h - 1}$ are the common differences of the arithmetic sequences H_j and h_k, respectively. A geometric sampling (linear sampling in the log space) is used for the L variable considering the rapid decay of the kernel function with respect to increasing distance between the source and the computation point.

Next the 3D array $\mathcal{K}_{g_z}^{tc}(L_i, H_j, h_k)$ obtained from discrete sampling is approximated using CP decomposition of rank N_{CP} as (see Fig. 1a):

$$\mathcal{K}_{g_z}^{tc}(L_i, H_j, h_k) \approx \sum_{n=1}^{N_{CP}} \lambda_n A_n(L_i) B_n(H_j) C_n(h_k), \tag{9}$$

then function values $\mathcal{K}_{g_z}^{tc}(L, H, h)$ at an arbitrary position within the region of interest can be obtained through a simple linear interpolation. Note that the linear interpolation is implemented in the log space for the L variable for improved numerical accuracy.

The function *cp_als* in the MATLAB Tensor Toolbox (Brett et al. 2021), which computes an estimate of the best rank-N CP model of a tensor using the well-known alternating least-squares algorithm (Kolda and Bader 2009), is used to obtain a discrete approximation of our kernel function. Figure 1 compares approximation errors by using CP tensor decomposition of rank 50 (Fig. 1c, f) and those from binomial expansion of order 6 with 48 terms (Fig. 1d, g) in a region of interest $[L, H, h] \in [1, 300] \times [0, 10] \times [0, 10] \, \text{km}^3$, representing a typical $2° \times 2°$ DEM dataset of the most mountainous area on the Earth. A small separating
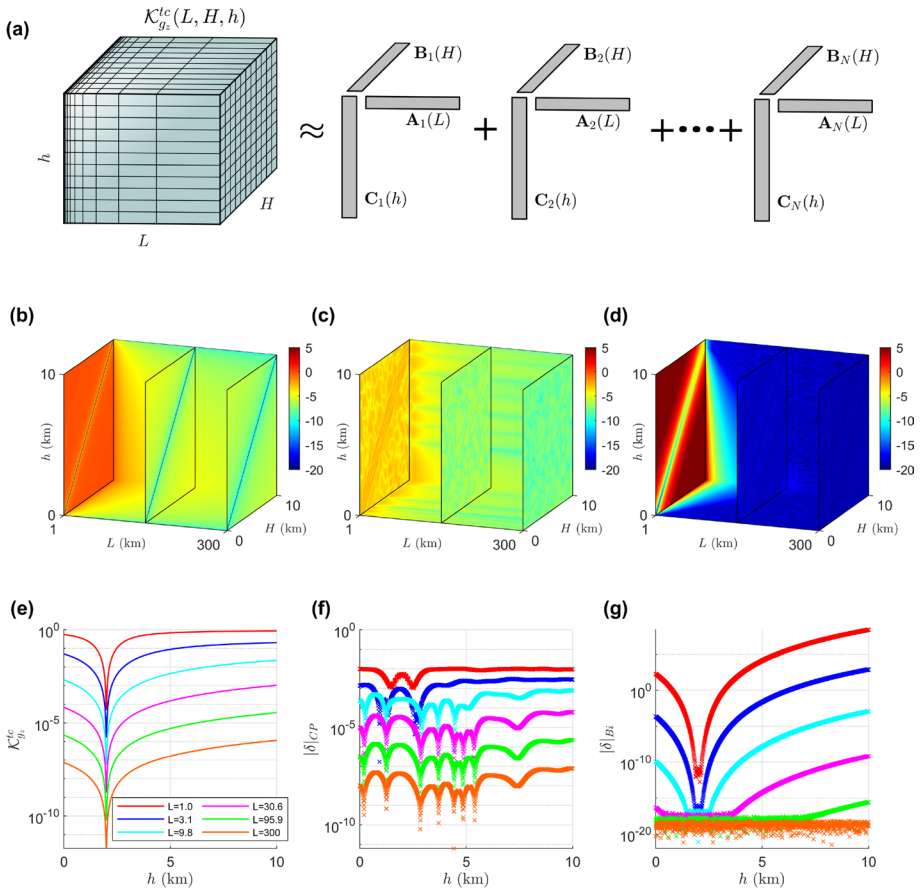
Fig. 1 a Illustration of the CP decomposition of the 3D kernel function $\mathcal{K}_{g_z}^{tc}(L, H, h)$ (redrawn from Kolda and Bader 2009, Fig. 3.1). The function $\mathcal{K}_{g_z}^{tc}$ is approximated using both CP decomposition of rank $N_{CP} = 50$ ($N_L = N_H = N_h = 100$) and binomial series of order $N_B = 6$ (with 48 terms) in the region of interest $[L, H, h] \in [1, 300] \times [0, 10] \times [0, 10]$ km^3. The 3D true function values are shown in **b** (in $\log_{10} |\mathcal{K}_{g_z}^{tc}|$ scale), with errors ($\log_{10} |\delta|$) of the CP decomposition and binomial series shown in **c** and **d**, respectively. The 1D true function values are shown in **e** by choosing a fixed value of $H = 2$ km and 6 different values of $L \in [1, 300]$ km. The corresponding errors for CP decomposition and binomial series are shown in **f** and **g**, respectively

radius $R_{FFT} = 1$ km is applied. It can be clearly observed that while the binomial expansion fails when $\left| \frac{H-h}{L} \right| > 1$, with errors well above the 10^0 level, the CP decomposition has errors below the 10^{-2} level in the entire region of interest.

Applying the CP decomposition, we have the outer zone effect reformulated as:

$$\bar{g}_z^{tc}(x, y, H) \approx G\rho \sum_{n=1}^{N_{CP}} \lambda_n B_n(H) \big[C_n(h) * A_n(L) \big], \tag{10}$$

with the convolution-type integrals $C_n(h) * A_n(L)$ evaluated efficiently using FFTs, $A_n(L)$ set to zero when $L < R_{FFT}$, and $B_n(H)$ moved outside the convolution integral since it is a

simple function of computation coordinates (x, y). In this way, convergence can be guaranteed even for a small separating radius R_{FFT}, which greatly speeds up the calculation of the inner zone effect using space-domain solutions. We call this new approach the CP-FFT algorithm.

2.3 CP-FFT for GP, GV, GGT Components with Laterally Variable Density

The CP-FFT algorithm can be easily extended to other gravitational components, and to the case of laterally variable density distributions. Considering the complete Bouguer effect of a DEM (here the "Bouguer plate" has a finite dimension equal to extension of the source DEM), for the constant density case, it can be obtained immediately from the terrain correction as:

$$g_z^{cb}(x, y, H) = g_z^{\Omega}(x, y, H) - g_z^{tc}(x, y, H), \tag{11}$$

where g_z^{Ω} represents the g_z effect caused by a rectangular prism with horizontal dimension equal to the integration area Ω, and vertical extension $[H, 0]$ changes according to the position of the computation point. For the more general case when horizontal density variations are allowed, however, it becomes more complicated to start from the terrain correction formulation. In this case, the complete Bouguer effect can be computed directly as:

$$g_z^{cb}(x, y, H) = G \int_{Y1}^{Y2} \int_{X1}^{X2} \rho(\tilde{x}, \tilde{y}) \left[\int_h^0 \frac{\partial}{\partial z} \left(\frac{1}{R} \right) d\tilde{z} \right] d\tilde{x} d\tilde{y}. \tag{12}$$

Solving the integration within the brackets leads to a new kernel function:

$$\mathcal{K}_{g_z}^{cb}(L, H, h) = \int_h^0 \frac{\partial}{\partial z} \left(\frac{1}{R} \right) d\tilde{z} = \frac{1}{\sqrt{L^2 + (H - h)^2}} - \frac{1}{\sqrt{L^2 + H^2}}. \tag{13}$$

Applying CP decomposition to $\mathcal{K}_{g_z}^{cb}$ we arrive at:

$$\bar{g}_z^{cb}(x, y, H) \approx G \sum_{n=1}^{N_{CP}} \lambda_n B_n(H) \Big(\left[\rho(\tilde{x}, \tilde{y}) C_n(h) \right] * A_n(L) \Big). \tag{14}$$

Here $A_n(L)$, $B_n(H)$ and $C_n(h)$ represent a CP decomposition of $\mathcal{K}_{g_z}^{cb}$ (Eq. 13). Obviously, they change according to different kernel functions. The density function $\rho(\tilde{x}, \tilde{y})$ is combined with $C_n(h)$ since both are functions of source coordinates $(\tilde{x}, \tilde{y})$. For brevity, we summarize kernel functions and their corresponding CP-FFT expressions for other gravitational components in Appendix 1.

2.4 Magnetic Terrain Effects

Once we have obtained the anomalous GGT:

$$\mathbf{\Gamma} = \begin{pmatrix} T_{xx} & T_{xy} & T_{xz} \\ T_{yx} & T_{yy} & T_{yz} \\ T_{zx} & T_{zy} & T_{zz} \end{pmatrix}, \tag{15}$$

the magnetic terrain effects can be obtained immediately through the Poisson's relation (Pedersen et al. 2015):

$$B_e = \frac{\mu_0}{4\pi} \frac{M}{G\rho} \hat{e}^T \boldsymbol{\Gamma} \hat{\boldsymbol{M}}, \tag{16}$$

where $\mu_0 = 4\pi \times 10^{-7}$ H/m is the magnetic permeability of free space, B_e is the anomalous magnetic field along the direction $\hat{e}$, ρ is the constant terrain density, $\hat{\boldsymbol{M}}$ and M are the unit direction and magnitude of the assumed homogeneous magnetization. In this case, only 6 GGT components need to be calculated by using the symmetric property of $\boldsymbol{\Gamma}$.

For a general case when the magnetization vector $\boldsymbol{M}$ changes arbitrarily throughout the region: $\boldsymbol{M} = \left(M_x(\tilde{x}, \tilde{y}), M_y(\tilde{x}, \tilde{y}), M_z(\tilde{x}, \tilde{y}) \right)$, which usually happens when both induced and remnant magnetizations are present (Liu et al. 2018), we have:

$$B_e = \hat{e} \cdot \boldsymbol{B}, \tag{17}$$

with $\boldsymbol{B} = (B_x, B_y, B_z)$ the anomalous magnetic vector that can be computed as:

$$B_x = \frac{\mu_0}{4\pi G} \left(T_{xx}^{M_x} + T_{xy}^{M_y} + T_{xz}^{M_z} \right), \tag{18}$$

$$B_y = \frac{\mu_0}{4\pi G} \left(T_{yx}^{M_x} + T_{yy}^{M_y} + T_{yz}^{M_z} \right), \tag{19}$$

$$B_z = \frac{\mu_0}{4\pi G} \left(T_{zx}^{M_x} + T_{zy}^{M_y} + T_{zz}^{M_z} \right). \tag{20}$$

Here $T_{xx}^{M_x}$, $T_{yx}^{M_x}$ and $T_{zx}^{M_x}$ represent the GGT components T_{xx}, T_{yx} and T_{zx} induced by a distribution of density $\rho(\tilde{x}, \tilde{y})$ equivalent to the magnetization component $M_x(\tilde{x}, \tilde{y})$, respectively. Other quantities can be understood analogously. In this case, a total of 9 GGT components (induced by 3 different variable density sources) need to be evaluated to compute the anomalous magnetic field.

2.5 Accelerating Inner Zone Computation Using a Gaussian Quadrature Mass Line (GQML) Model

The CP-FFT algorithm derived above offers a fast and stable computation of the outer zone effect. However, even for a small separating radius of $R_{FFT} = 2$ km, a direct evaluation of the analytical prismatic solution (Nagy et al. 2000) may still be time-consuming for computing high-resolution DEMs (e.g., 90 m resolution or higher). A numerical quadrature solution based on the trapezoidal and Simpson's rules that is sufficiently accurate with respect to the exact analytical prismatic solution, but which can reduce the computation time by almost 50 per cent is introduced in Goyal et al. (2020). Here we apply a Gaussian quadrature mass line (GQML) model with variable order according to different horizontal distances between the computation point and the integration element. The GQML model is simply to carry out the 3D volume integrals of the gravitational kernels using analytical integration along the vertical dimension, and 2D Gaussian quadrature along the two horizontal dimensions. The idea is similar to the algorithm used in Goyal et al. (2020), we made a modification by applying Gaussian quadrature instead of trapezoidal or Simpson quadratures, and extended to all gravitational components.

Figure 2 shows details of the GQML model for each computation point (indicated by a red star) for a typical mid-latitude SRTM v4.1 DEM data with spatial resolution $a = 90$ m (along south-north direction), and $b = a \cos(30°) \approx 80$ m (along west-east direction). Depending on the distance R from the center of a grid cell to the computation point, the closest zone with $R < R_1 = a$ is calculated using directly the rigorous prismatic analytical solution (yellow rectangles, normally only 3 prisms needs to be calculated). Gaussian quadrature of orders $N_{GQ} = 4^2 = 16$, $N_{GQ} = 2^2 = 4$ and $N_{GQ} = 1^2 = 1$ are used to approximate the prismatic analytical solution in the near zone $R \in [R_1, R_2) = [a, 3a)$ (dark blue), intermediate zone $R \in [R_2, R_3) = [3a, 10a)$ (blue), and distant zone $R \in [R_3, R_{FFT}) = [10a, R_{FFT})$ (light blue), respectively. The region with $R \geq R_{FFT} = 2$ km is computed by the CP-FFT algorithm (red zone).

Figure 3 shows changes in relative errors $|\epsilon|$ of the Gaussian quadrature mass line (GQML) model in approximating the analytical prismatic solution of g_z with respect to several parameters, including (1) the distance/length ratio L/a, (2) height/length ratio of the prism c/a, and (3) order of the GQML N_{GQ}. It can be observed that by choosing the
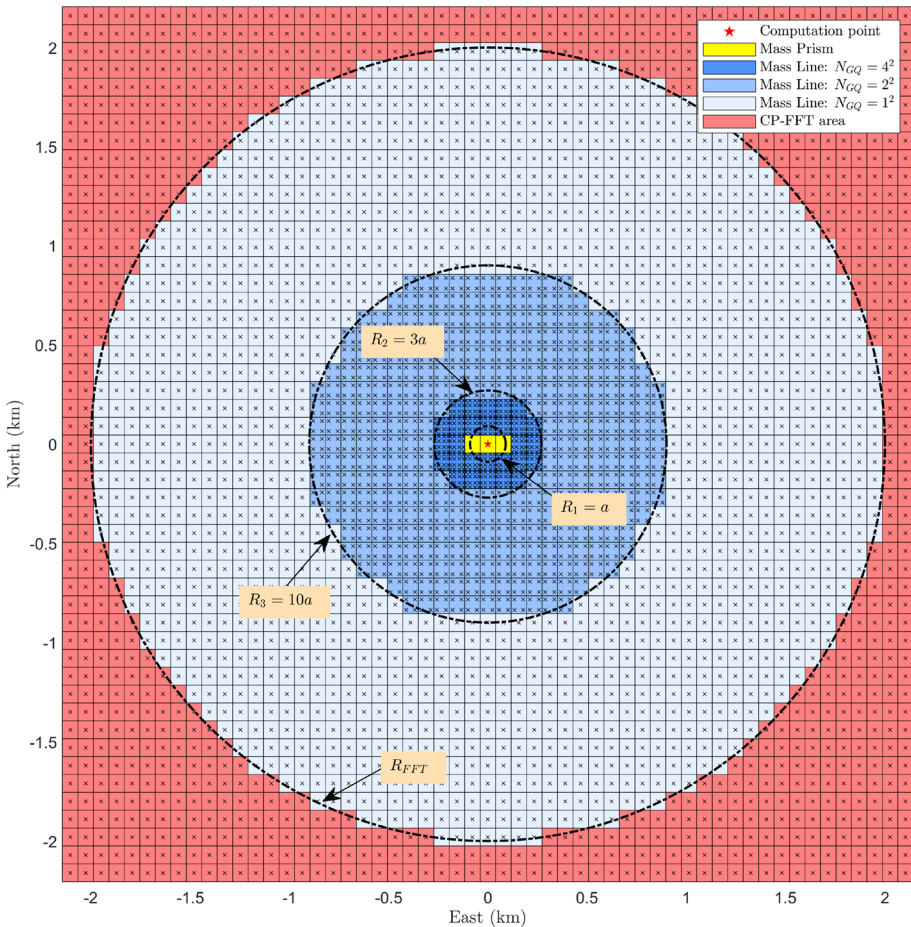

Fig. 2 Gaussian quadrature mass line (GQML) approximation of the mass prism model

parameters described above, generally a relative error of $|\epsilon| \leq 10^{-3}$ can be guaranteed for prismatic bodies with various geometries (a height/length ratio of $c/a = 100$ represents a prism with length 90 m and height 9000 m, while a height/length ratio of $c/a = 0.1$ represents a prism with length 90 m and height 9 m, the width of the prism is fixed as $b \approx 80$ m as has been mentioned above).

Numerical behavior of the GQML approximation for other gravitational components, including the GP, the other two GV components, and the GGT components are similar. Smaller relative errors are obtained for the GP component (generally below 10^{-4}), and larger relative errors $|\epsilon| > 10^{-2}$ occur for GGT components only when the magnitude of the referenced value is very small ($< 10^{-3}$ Eötvös), thus is negligible in a practical modeling procedure. Based on these numerical results, we have chosen the same set of GQML model parameters for all gravitational components.

3 Numerical Examples and Results

We test the numerical performance of our CP-FFT method by using space-domain mass line (Li and Sideris 1994) or mass prism solutions (Nagy et al. 2000) as the precise references. The l_2-norm relative error E_2 is applied as an overall estimation of the numerical accuracy (Wu 2021). Computational time costs t_{ref} and t_{cp} for both methods, together with the acceleration ratio $\tau = t_{ref}/t_{cp}$, are provided for verification of numerical efficiency. It should be noted that the computer code for space-domain solutions have also been properly optimized to achieve maximum speed. The experiments are carried out on a platform with Intel Core $i7 - 9850H$ 2.6 GHz and 64 GB RAM, and implemented in MATLAB R2020b software.

Numerical experiments are arranged as follows: (1) In Sect. 3.1, we use a simple mass line model (SML) to test the accuracy and efficiency of our CP-FFT method for outer-zone computation, as for the inner-zone computation, both methods apply the space-domain mass line solution. Based on the numerical results obtained in Sect. 3.1, we carry out further numerical tests in Sect. 3.2 and provide empirical choice for parameters of our algorithm for different topographic models. (2) In Sect. 3.3, we take a step further to include a Gaussian quadrature mass line (GQML) model for inner-zone computation, and compare our method to the more rigorous rectangular prism solution. Therefore, numerical approximations are made for both inner/outer-zone calculations. Computation surfaces, both on, above and below the topography are tested. (3) In Sects. 3.4 an 3.5, numerical examples are designed to demonstrate the validity of our algorithm for computing terrain-induced terrestrial and airborne gravitational effects, including all GP, GV and GGT components, and for magnetic terrain effects, with variable density/magnetization taken into account.

3.1 Simple Mass Line (SML) Model Tests

First we test our new algorithm using a simple mass line (SML) model, where each prismatic grid cell is approximated using a single mass line at its center. Four patches of $2° × 2°$ SRTM v4.1 data with $3'' × 3''$ resolution (Jarvis et al. 2008), including Himalayas, Andes, European Alps and Australian Alps, are used as the input topographic data source. Planar approximations are applied by letting $\Delta x = 3''\chi$, $\Delta y = 3''\chi \cos(\varphi_m)$, where φ_m is
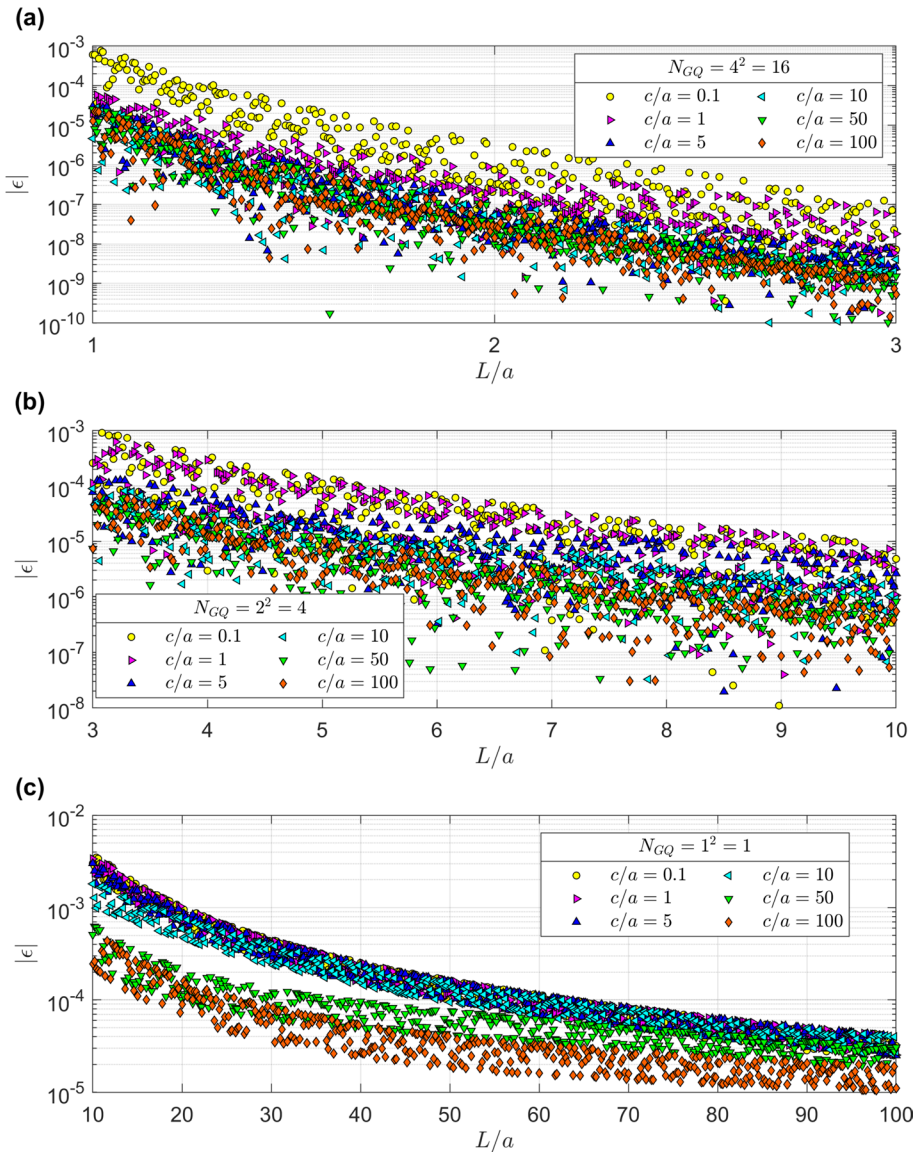
Fig. 3 Change in relative errors $|\epsilon|$ with respect to distance/length ratio L/a, height/length ratio of the prism c/a, and different orders N_{GQ} of the Gaussian quadrature mass line (GQML) model in approximating the analytical prismatic solution of g_z

the mean latitude of the patch and χ is the arcseconds-to-kilometres conversion factor for a sphere of radius $R_e = 6378.137$ km. A constant density $\rho = 2670$ kg/m^3 is assumed.

We apply CP decomposition to the terrain correction kernel $\mathcal{K}_{g_z}^{tc}$ (Eq. 5), the complete Bouguer effects are calculated by adding to the terrain correction effects the contribution of a "regional prism" (see Eq. 11). Parameters of the CP-FFT algorithm are chosen as $N_L = N_H = N_h = 100$, $R_{FFT} = 2$ km, and $N_{CP} = 50$. Gravity values are calculated right above the topography. As shown in Fig. 4, almost identical forward results are obtained, with maximum absolute errors (MAEs) below 1 mGal, root mean square (RMS) errors below 0.15 mGal, and E_2 errors below 0.1% for all selected mountainous regions. More statistical details of the results are summarized in Table 1. The space-domain solution takes more than 20 days to complete the whole calculation (4 patches, each with source grid 2400×2400, computation grid 2160×2160). The CP-FFT algorithm, on the other hand, costs only about 9 minutes (acceleration $\tau > 3000$), proving its huge advantage in computational efficiency.

3.2 Empirical Choice for the Parameters of the CP-FFT Algorithm

Although we have chosen parameters of the CP-FFT algorithm as $R_{FFT} = 2$ km and $N_{CP} = 50$ in all numerical tests implemented above, it should be noted that for a DEM with less change in height values, a lower rank of CP decomposition (N_{CP}) and a smaller separating radius (R_{FFT}) may be adequate to provide forward results with sufficiently high accuracy in less computation time.

Figure 5 shows changes in maximum absolute errors (MAE) and root mean square (RMS) errors (in mGal) with respect to different separating radius and increasing CP decomposition ranks for the modeling of the gravitational component g_z caused by the chosen 4 test areas around the globe with different topographic elevation differences: (a) Himalayas (about 9 km), (b) Andes (about 6 km), (c) European Alps (about 4.5 km) and (d) Australian Alps (about 2 km). The numerical results can be summarized as follows:

i)   Increasing the separating radius (R_{FFT}) always improves accuracy, albeit at the computational expense of more time-consuming space-domain inner zone evaluation.

ii) Ideally, convergence should be guaranteed no matter what R_{FFT} is chosen. However, it can be observed in Fig. 5 that when R_{FFT} is chosen small comparing to the overall height change in the DEM, e.g., $R_{FFT} = 1$ km for the Himalayas region, convergence of the algorithm slow down significantly. This may be caused by the intrinsic difficulty in approximating the gravitational kernel for near-field effect using CP decomposition.

iii) Increasing the rank of CP decomposition (N_{CP}) generally also improves the accuracy, however, the accuracy no longer improves after a certain threshold is reached. Besides, due to the randomness of the CP decomposition, some irregular jumps of the MAE and RMS errors can be observed, but the overall trend is not affected.

iv) The results in Fig. 5 can serve as a reference for parameter selection criterion of the CP-FFT algorithm for computing terrain-induced gravitational fields in other mountainous regions. We recommend a selection of $R_{FFT} = \frac{\max(h) - \min(h)}{4}$, and $N_{CP} = 50$, for which MAE below 1 mGal, and RMS below 0.1 mGal can be achieved.

To explore more convergence characteristics of the CP-FFT method, we carried out further numerical tests using an extreme value of the parameter $R_{FFT} = 0.05$ km in the Himalayas test area. In this case, even the nearest mass line element (at a distance about
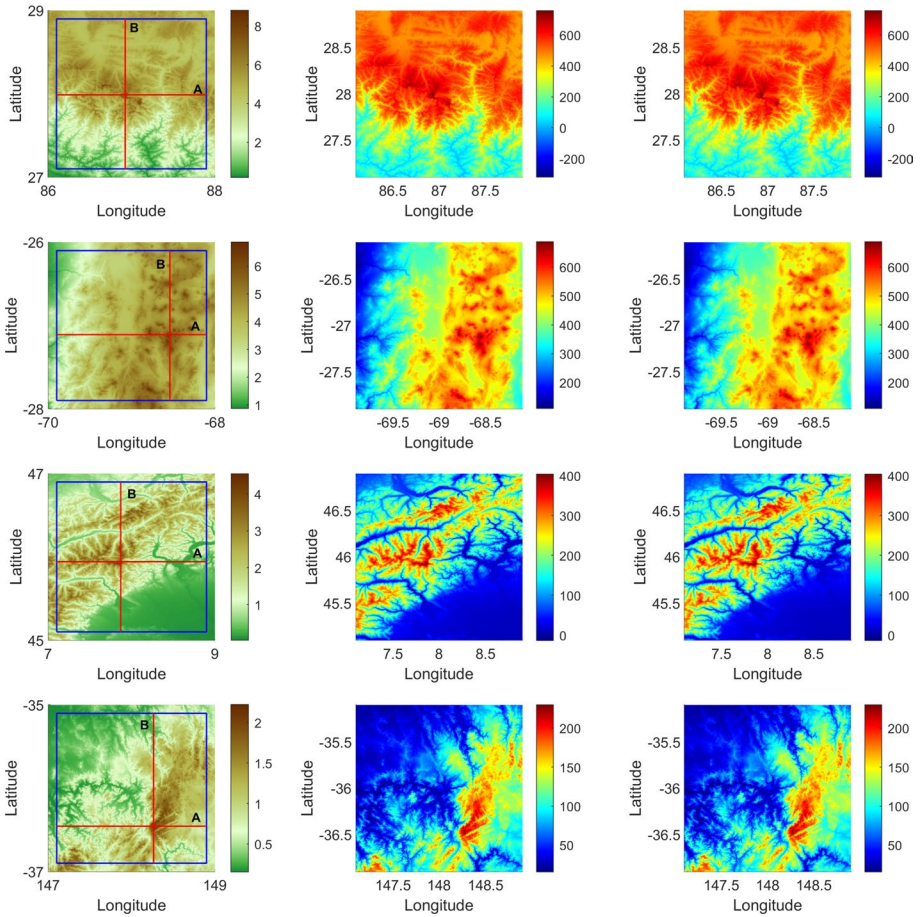
Fig. 4 DEMs (first column, unit in km) and the corresponding forward results of g_z^{cb} (in mGal) over 4 selected mountainous areas around the globe using space-domain rigorous solution of mass lines (second column) and the CP-FFT algorithm (third column). Test areas include Himalayas (first row), Andes (second row), European Alps (third row) and Australian Alps (fourth row). Blue rectangles indicate calculation areas, red lines indicate two profiles (A and B) crossing the highest peaks of each test area

0.08 km) is excluded from the inner-zone calculation for each computation point, which means we now have a pure FFT algorithm over the entire region. We also choose three different values of $N_{LHh} = 100, 200, 300$, where $N_{LHh} = N_L = N_H = N_h$ is the dimension of the CP decomposition, to test the effect of this parameter on the final accuracy.

Figure 6 shows error level changes as the rank of CP decomposition N_{CP} increases from 100 to 1000, and dimension of the CP decomposition N_{LHh} increases from 100 to 300. We summarize the numerical results as follows:

(i) Ideally, for the same computation area, larger values of N_L, N_H, N_h would provide more accurate results. However, numerical tests show that the approximation accuracy reaches a certain limit when the values of N_L, N_H, N_h are large enough. After that, further increasing the value cannot effectively reduce the error, but brings more

Table 1 Descriptive statistics of the topography height values, the forward results of g_z^{cb} calculated using both the mass line analytical solution (reference) and the CP-FFT algorithm, with the corresponding differences between the two algorithms over 4 selected test areas shown in Fig. 4. Elevation values in km (positive upward), g_z^{cb} values in mGal

Test area	Quantity	Min	Max	Mean	RMS	E_2
Himalayas	Elevation	0.179	8.806	3.840	4.180	0.030%
	Reference	−320.771	758.460	405.823	441.030	
	CP-FFT	−320.978	757.914	405.735	440.965	
	Difference	−0.617	0.275	−0.088	0.130	
Andes	Elevation	0.869	6.868	3.848	4.000	0.010%
	Reference	109.469	688.475	424.215	437.389	
	CP-FFT	109.469	688.386	424.173	437.349	
	Difference	−0.152	0.011	−0.042	0.044	
European Alps	Elevation	0.032	4.550	1.285	1.586	0.025%
	Reference	−13.722	404.283	133.753	164.066	
	CP-FFT	−13.783	404.161	133.714	164.034	
	Difference	−0.142	0.011	−0.038	0.040	
Australian Alps	Elevation	0.156	2.220	0.759	0.864	0.010%
	Reference	15.558	229.732	84.155	95.329	
	CP-FFT	15.541	229.706	84.146	95.321	
	Difference	−0.040	0.000	−0.009	0.010	

computation. The inherent randomness of the CP decomposition function *cp_als* brings some uncertainty, larger parameters do not necessarily give better results, it may even reduce the accuracy in some cases.

(ii) The pure FFT method converges rather slowly, even by using a large value of $N_{CP} = 1000$, we still have MAEs and RMS errors above 1 mGal in all cases. This suggests that by applying the current CP decomposition algorithm, we still can not obtain an accurate global approximation of the gravitational kernel. Therefore, inner-zone computation using space-domain solution is still necessary to guarantee a sub-mGal level accuracy in the most mountainous areas of the Earth.

We also made a rough estimate of the computation time of our CP-FFT algorithm as a function of grid sizes, CP decomposition rank, and the separating radius based on the results obtained above. As shown in Fig. 7, computation time increases linearly with N_{CP}, and quadratically with R_{FFT}, the relation can be estimated as:

$$t = c_0 + c_1 \hat{N} \log(\hat{N}) N_{CP} + c_2 \frac{N_x N_y}{\Delta x \Delta y} R_{FFT}^2, \tag{21}$$

where $\hat{N} = (N_x + \tilde{N}_x)(N_y + \tilde{N}_y)$ is the size of the 2D FFT implemented in calculating the outer-zone effect, $\tilde{N}_x \times \tilde{N}_y$ is the size of the topographic source grid, $N_x \times N_y$ is the size of the computation grid, $\Delta x \times \Delta y$ is the dimension of a grid cell, and $\frac{N_x N_y}{\Delta x \Delta y} R_{FFT}^2$ is proportional to the number of mass lines required in evaluating the inner-zone effect for an SML model.

The estimated values for c_0, c_1 and c_2 given by a least square fitting are: $c_1 \approx 5.2 \times 10^{-9}$, $c_2 \approx 1.6 \times 10^{-8}$, and $c_0 \approx 2.5$ on our platform. We mention that for the GQML model
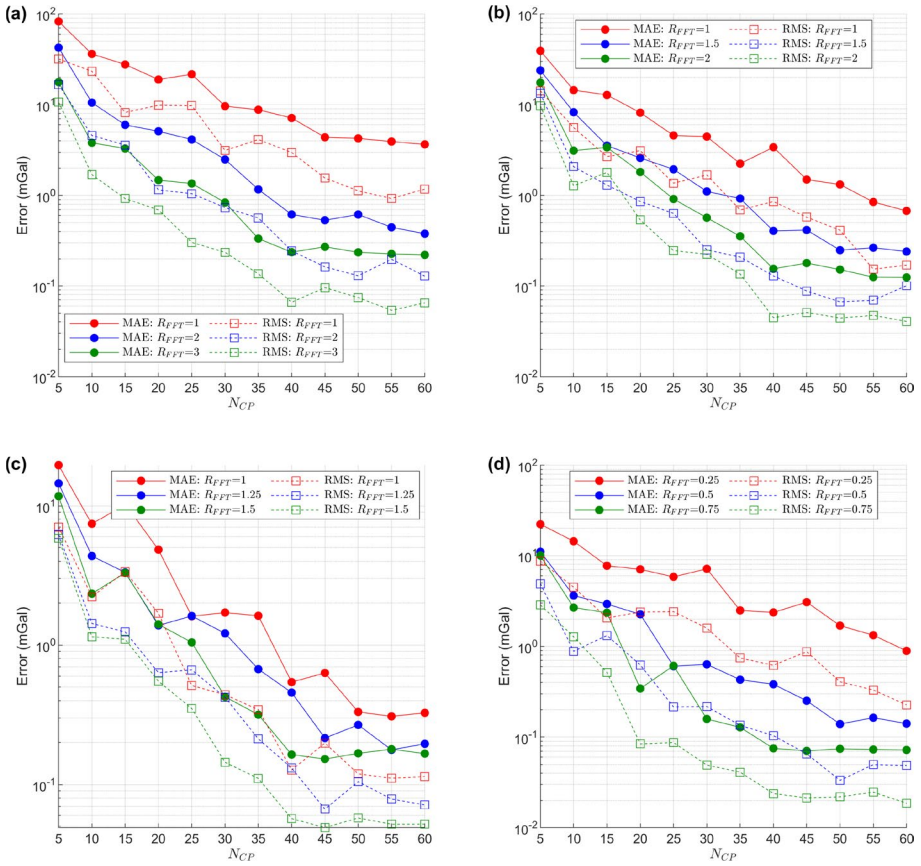
Fig. 5 Error level changes with respect to increasing rank of CP decomposition N_{CP} and different separating radius R_{FFT} (in km) for the modeling of g_z field induced by the chosen 4 test areas: **a** Himalayas, **b** Andes, **c** European Alps and **d** Australian Alps. MAE stands for maximum absolute error, RMS stands for root mean square error

implemented in the following, the computation amount does not change for the outer-zone evaluation, however, the number of mass lines required for the inner-zone computation would be approximately 1 to 3 times larger than that of the SML model. Therefore, a rough estimation of $c_2^{GQML} \approx 2c_2^{SML}$ can be applied for time estimation of a CP-FFT algorithm combined with a GQML approximation of the mass prism model.

3.3 Gaussian Quadrature Mass Line Model Tests

Next we evaluate the analytical prismatic solution (Nagy et al. 2000) as the precise reference, and combine our CP-FFT algorithm with a Gaussian quadrature mass line (GQML) model to speed up the inner zone computation with controlled accuracy. Each prismatic grid cell is now approximated using multiple mass lines formulating a 2D Gaussian quadrature. Depending on the attenuation of the gravitational fields with distance, the order of the Gaussian quadrature is chosen as $N_{GQ} = 16$, 4, and 1 in the near,
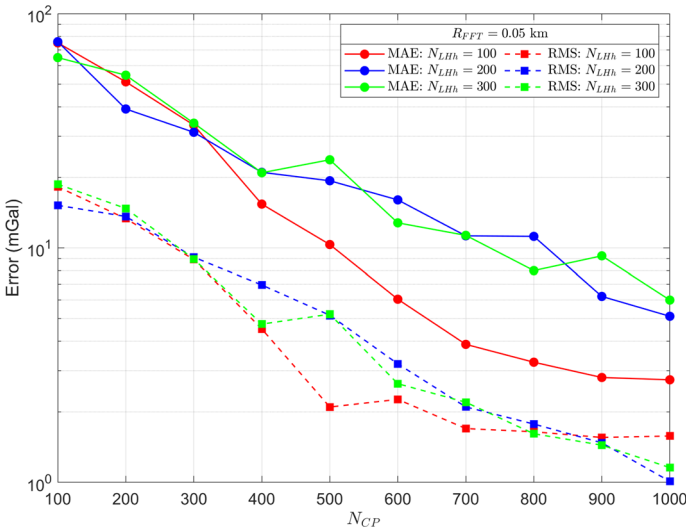
Fig. 6 Error level changes with respect to increasing rank of CP decomposition N_{CP} using a pure FFT algorithm in the Himalayas test area. Here $R_{FFT} = 0.05$ km is chosen to completely avoid the analytical calculation of the inner-zone effect. MAE stands for maximum absolute error, RMS stands for root mean square error

intermediate and distant zone, respectively, to guarantee a relative error of $|\epsilon| \leq 10^{-3}$ (see Fig. 2).

As shown in Fig. 8, g_z^{cb} effects of the Himalayas test area are calculated and compared on 8 different observation heights parallel to the topography with distance $D = 0, 500, 1000, 2000, -500, -1000, -2000, -5000$ m (positive/negative D indicate computation surface above/below the topography). The CP-FFT method is implemented using directly the CP decomposition of the $\mathcal{K}_{g_z}^{cb}$ kernel (Eq. 13). The prism-summation (PS) solution is computed only along two profiles (A and B in Fig. 4) for reference due to the enormous computational costs. Almost identical forward results are obtained, with MAEs below 2 mGal, RMS errors below 0.5 mGal, and E_2 errors below 0.2% for all chosen observation heights. More statistical details can be found in Table 2. The space-domain solution takes more than 16 hours computing results simply on two profiles, while the CP-FFT algorithm takes only about 36 minutes computing all 8 observation surfaces (acceleration $\tau > 20000$), showing its capability for high-efficiency computation of terrain-induced gravitational fields on arbitrary undulating surfaces.

Similar comparisons are made for the T_{zz}^{cb} component on two profiles crossing the highest peak of the European Alps test area at various heights $D = 1, 5, 10, 50, 100, 500, 1000, 5000$ m above the topography. As shown in Fig. 9, again, almost identical forward results are obtained, with MAEs below 2 Eötvös, RMS errors below 1 Eötvös, and E_2 errors below 0.3% for all chosen observation heights. More statistical details can be found in Table 3. The space-domain solution takes about 4.5 hours computing results simply on two profiles, while the CP-FFT algorithm takes only about 1 hour computing all 8 observation surfaces. Here an acceleration ratio of $\tau > 5000$ is achieved. Comparing with the time costs for computing g_z^{cb}, space-domain solution accelerates about 3 times due to simpler expressions (Nagy et al. 2000), while the CP-FFT solution slows down slightly due to increased complexity of the analytical mass line expressions (see Appendix 1, J_1 and J_2 expressions).
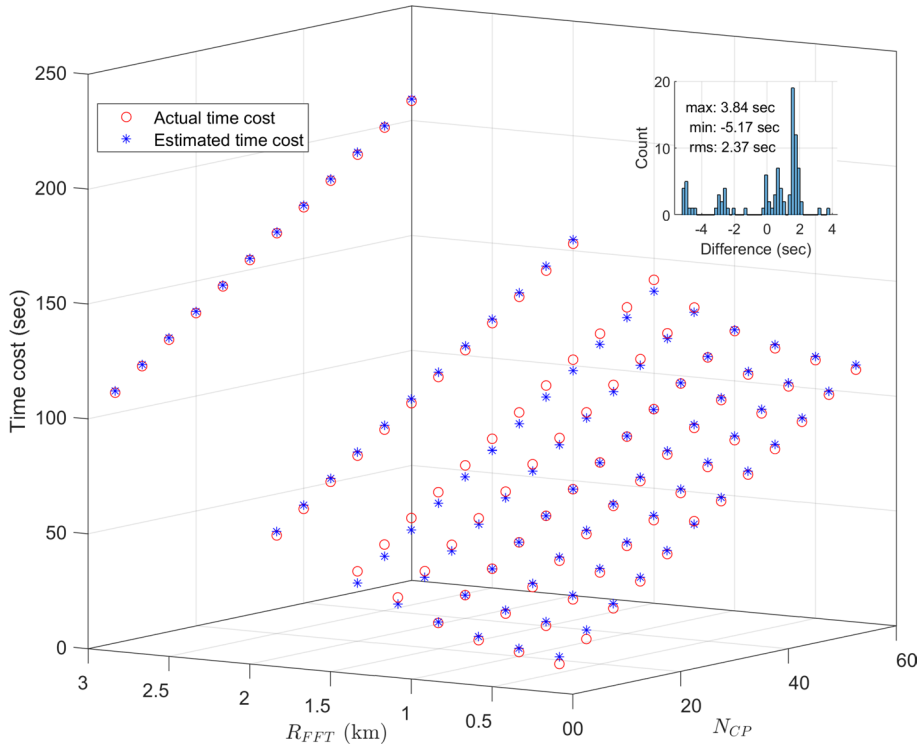
Fig. 7 Time costs of the CP-FFT algorithm estimated as a function of the rank of CP decomposition N_{CP} and the separating radius R_{FFT}, with estimation errors and associated statistics (minimum, maximum and root-mean-square) shown in the histogram

3.4 GP, GV and GGT Modeling with Laterally Variable Density

We now test our CP-FFT algorithm for a complete modeling of GP, GV, GGT components caused by a large DEM with laterally variable density. As shown in Fig. 10, the area bordered by latitude 35°N to 40°N and longitude 110°W to 102°W, which was applied in the Colorado 1-cm geoid computation experiment (Wang et al. 2021) for a comparison study of numerous geoid computation methods used by different groups around the world, is adopted here for numerical validation.

The input topographic dataset is the SRTM v4.1 DEM with a spatial resolution of 3″ and a total grid size of 9601 × 6001. The input 3″ resolution laterally variable density grid is obtained from linear interpolating the 30″ resolution UNB_TopoDens model (Sheng et al. 2019), which is transformed from the Global Lithology Model (GLiM) (Hartmann and Moosdorf 2012) by assigning probable surface density values to the lithologies based on geological data. The density value varies between a minimum of 1000 kg/m³, indicating lakes within the area, and a maximum of 2854 kg/m³, slightly above the normally applied mean topographic density value 2670 kg/m³ (see Fig. 10b). It should be noted that since vertical variation of density is not considered, the laterally variable density model used here is more to validate our algorithm than as a better approximation to the real density distribution.
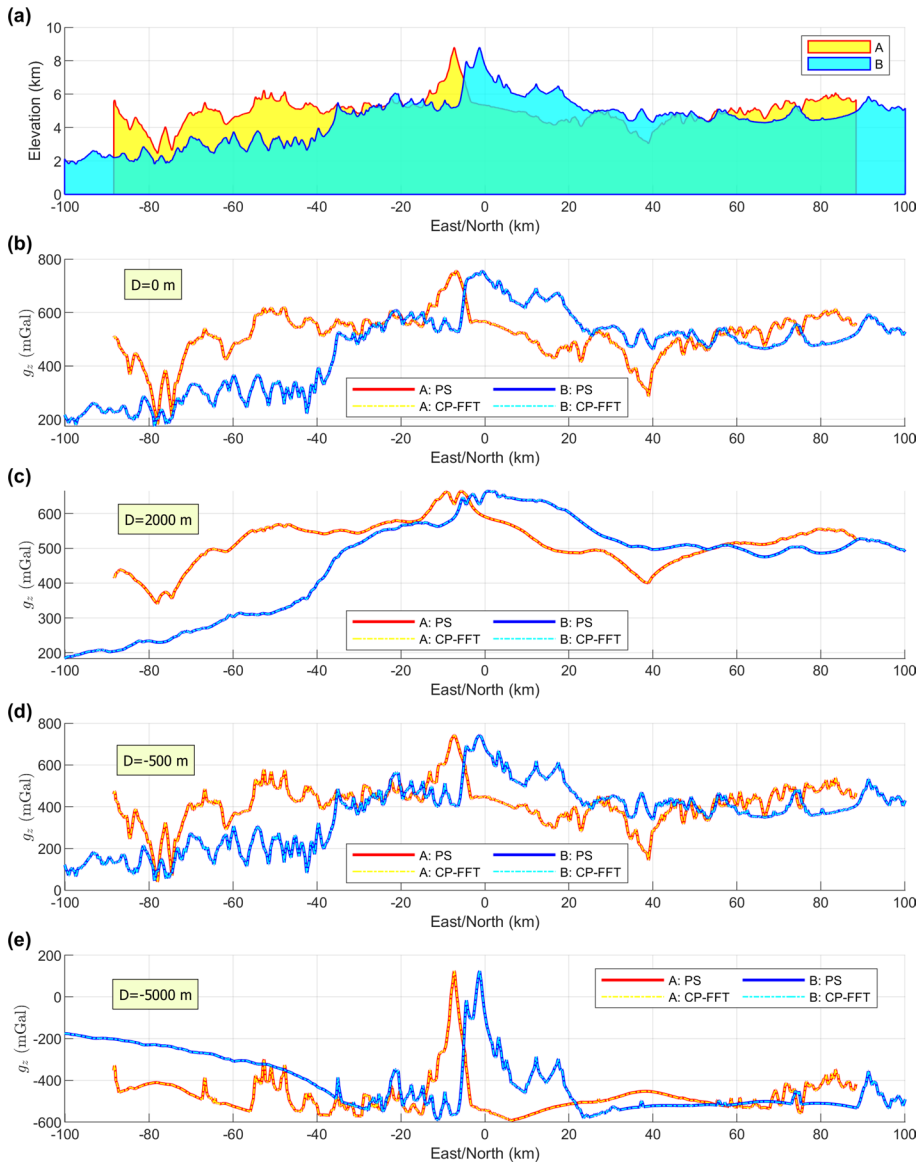
Fig. 8 Forward results of g_z^{cb} on two profiles crossing the highest peak of the Himalayas test area with multiple computation heights D. **a** Elevation changes along the two profiles (red lines A and B in Fig. 4, first row). Forward results using both the rigorous prism-summation (PS) method (red and blue solid lines) and the CP-FFT method (yellow and cyan dash-dot lines) are compared on 8 different observation heights (only 4 are shown here) parallel to the topography with a distance D, with **b** $D = 0$ m representing the topography itself, **c** $D = 2000$ m simulating typical flight heights for airborne surveys, and **d** $D = -500$ m, **e** $D = -5000$ m indicating underground computation profiles. Statistical details for all 8 computation heights are summarized in Table 2

As shown in Fig. 10a, a subset of 7991 gravity observations, with 3906 terrestrial ones and 4085 airborne ones (randomly picked with generally equal distance), are selected from

Table 2 Descriptive statistics of the forward results of g_z^{cb} in Fig. 8. Comparisons are made on 8 different observation heights parallel to the topography, with $D = 0$ m representing the topography itself, $D = 500, 1000, 2000$ m above the topography, and $D = -500, -1000, -2000, -5000$ m below the topography. Gravity values in mGal

Observation height	Quantity	Min	Max	Mean	RMS	E_2
$D = 0$ m	Reference	174.547	755.716	490.052	504.841	0.070%
	CP-FFT	174.523	756.010	490.178	504.950	
	Difference	−1.673	1.465	0.127	0.351	
$D = 500$ m	Reference	199.132	727.314	493.247	506.871	0.083%
	CP-FFT	199.613	728.520	493.532	507.163	
	Difference	−0.922	1.222	0.285	0.418	
$D = 1000$ m	Reference	197.607	703.028	492.451	505.534	0.077%
	CP-FFT	197.715	703.646	492.775	505.871	
	Difference	−0.301	0.913	0.323	0.391	
$D = 2000$ m	Reference	183.740	664.455	487.122	499.713	0.061%
	CP-FFT	183.892	664.756	487.276	499.885	
	Difference	−0.565	0.711	0.154	0.306	
$D = -500$ m	Reference	40.453	742.655	388.925	409.459	0.064%
	CP-FFT	40.631	741.810	388.919	409.476	
	Difference	−0.913	1.023	−0.006	0.264	
$D = -1000$ m	Reference	−81.798	717.877	284.952	314.925	0.085%
	CP-FFT	−81.949	717.390	285.141	315.132	
	Difference	−0.487	0.876	0.188	0.267	
$D = -2000$ m	Reference	−313.969	618.074	74.230	161.252	0.185%
	CP-FFT	−313.864	619.209	74.269	161.409	
	Difference	−0.733	1.142	0.039	0.298	
$D = -5000$ m	Reference	−593.078	124.038	−440.795	456.699	0.114%
	CP-FFT	−593.712	123.980	−441.255	457.195	
	Difference	−0.883	0.210	−0.461	0.520	

the gravity datasets used in the Colorado geoid computation experiment (Wang et al. 2021). For the terrestrial gravity dataset, only observations above the input DEM (with terrain clearance $D = H_{cal} - h_{DEM} \geq 0$) are kept. Nevertheless, we still get D values vary from 0 m to a maximum of 535 m, which is clearly unrealistic for land gravity observations. These may be caused by height errors from either the DEM or the gravity dataset, we leave these unchanged to cover forward modeling situations when airborne surveys are carried out on a typical height of several hundred meters above topography in flat areas (Pedersen et al. 2015). For airborne observations, terrain clearance D changes vastly from about 1300 m to 6400 m, which is more than adequate to cover most practical airborne modeling situations.

The calculation surface H_{cal} (see Fig. 10d) is constructed as follows: first the terrain clearance values D of the picked 7991 gravity observations are interpolated to a regular grid identical to the DEM dataset using a nearest-neighbor method (see Fig. 10c), then the calculation surface is obtained from $H_{cal} = h_{DEM} + D$, where h_{DEM} denotes the DEM height of the grid point, and D is the interpolated terrain clearance value at the grid point.

The CP-FFT method is applied for the computation of all GP, GV and GGT components on the undulating calculation surface. Due to the increased horizontal extents
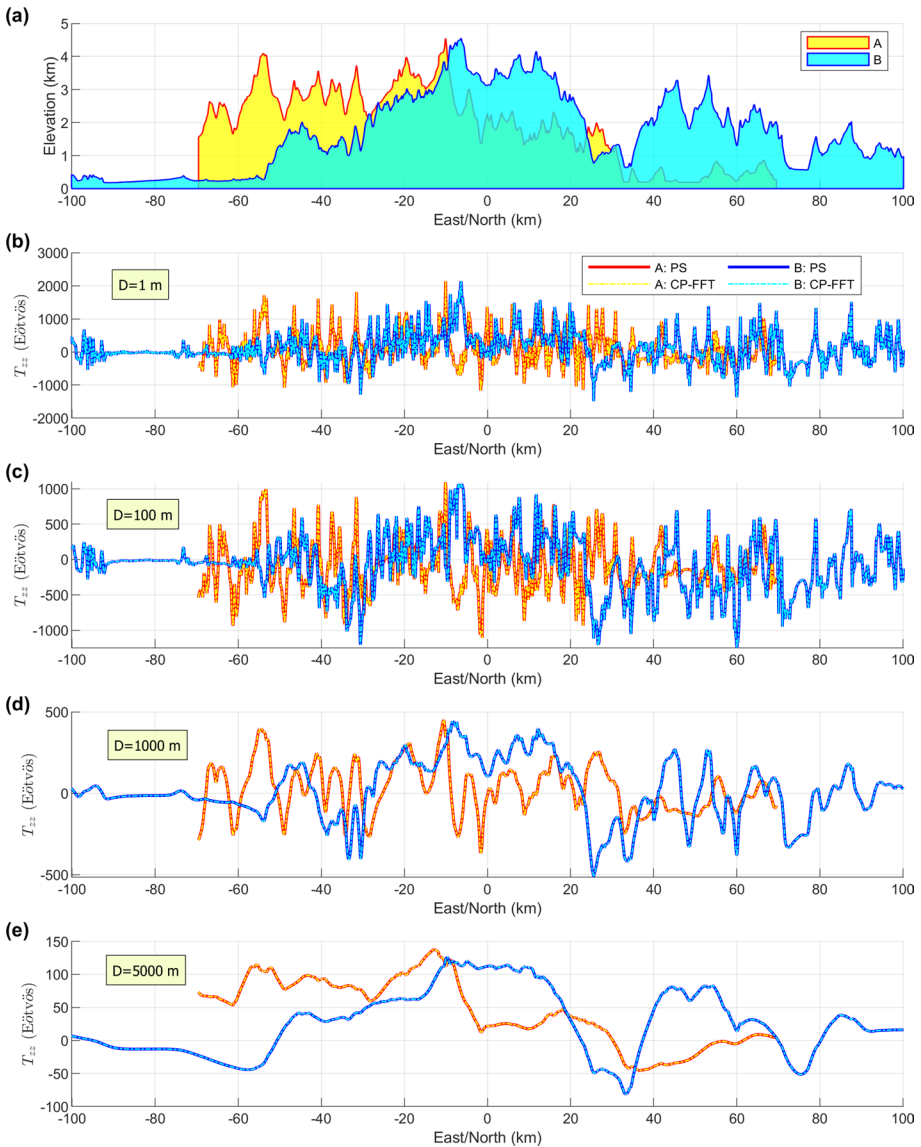
Fig. 9 Forward results of T_{zz}^{cb} on two profiles crossing the highest peak of the European Alps test area with multiple computation heights D. **a** Elevation changes along the two profiles (red lines A and B in Fig. 4, third row). Forward results using both the rigorous prism-summation (PS) method (red and blue solid lines) and the CP-FFT method (yellow and cyan dash-dot lines) are compared on 8 different observation heights (only 4 are shown here) parallel to the topography with a distance D, with **b** $D = 1$ m above the topography, **c** $D = 100$ m, **d** $D = 1000$ m and **e** $D = 5000$ m simulating typical flight heights for airborne surveys. Statistical details for all 8 computation heights are summarized in Table 3

Table 3 Descriptive statistics of the forward results of T_{zz}^{cb} in Fig. 9. Comparisons are made on 8 different observation heights parallel to the topography, with $D = 1, 5, 10, 50, 100, 500, 1000, 5000$ m all above the topography. Units in Eötvös

Observation height	Quantity	Min	Max	Mean	RMS	E_2
$D = 1$ m	Reference	−1493.906	2144.877	97.296	459.919	0.130%
	CP-FFT	−1494.734	2144.979	96.761	459.849	
	Difference	−1.184	0.103	− 0.534	0.599	
$D = 5$ m	Reference	−1525.823	2058.288	54.333	444.749	0.135%
	CP-FFT	−1526.649	2058.389	53.796	444.738	
	Difference	−1.184	0.101	−0.537	0.601	
$D = 10$ m	Reference	−1551.856	1948.852	4.796	433.245	0.139%
	CP-FFT	−1552.677	1948.947	4.259	433.305	
	Difference	−1.191	0.095	−0.537	0.602	
$D = 50$ m	Reference	−1406.943	1339.346	−121.034	415.544	0.145%
	CP-FFT	−1407.882	1339.381	−121.570	415.797	
	Difference	−1.186	0.083	−0.536	0.603	
$D = 100$ m	Reference	−1248.256	1092.116	−81.804	367.956	0.163%
	CP-FFT	−1249.093	1092.070	−82.341	368.180	
	Difference	−1.148	0.053	−0.537	0.600	
$D = 500$ m	Reference	−759.305	661.659	−3.332	236.778	0.253%
	CP-FFT	−760.190	661.288	−3.868	236.981	
	Difference	−1.268	0.717	−0.536	0.599	
$D = 1000$ m	Reference	−513.635	450.109	23.614	167.839	0.223%
	CP-FFT	−514.608	450.173	23.327	167.983	
	Difference	−1.032	0.685	−0.287	0.374	
$D = 5000$ m	Reference	−80.870	137.892	34.857	61.312	0.118%
	CP-FFT	−80.899	138.015	34.906	61.379	
	Difference	−0.029	0.141	0.049	0.072	

of both the source and the computation grids, and the large vertical extent of the observations ($H_{cal} \in [1028, 9195]$ m), parameters of the CP-FFT algorithm are chosen as $N_L = N_H = N_h = 200$, $R_{FFT} = 2$ km, and $N_{CP} = 60$ here. The obtained g_z and T_{zz} components are shown in Fig. 10e and f, respectively. It can be observed that g_z field in the airborne region (red zone in Fig. 10c) is somehow a low-pass filtered version of the terrestrial field (blue zone in Fig. 10c), and both have a strong correlation with the DEM. The T_{zz} component, which is a high-pass filtered version of the g_z filed, clearly contains more short-wavelength information, especially for the terrestrial observations. (Note here we choose limits $[−100, 100]$ Eötvös for the color bar to show more details of the T_{zz} field, the actual limits are $[−1100, 1462]$ Eötvös, see Table 4).

For precise reference, the prism-summation (PS) solution is computed at the selected 7991 gravity observations (see Fig. 10a). Figure 11 shows difference maps of all GP, GV and GGT components between the two applied algorithms at the selected observations. More statistical details are summarized in Table 4. Obviously, the two algorithms agree perfectly, with E_2 errors below 0.01%, 0.1% and 1.3% for the GP, GV and GGT components, respectively. Specifically, we have MAE as 0.1 mGal, RMS error as 0.05 mGal, E_2 error as 0.02% for the g_z component, and MAE below 1 Eötvös, RMS error below 0.1 Eö
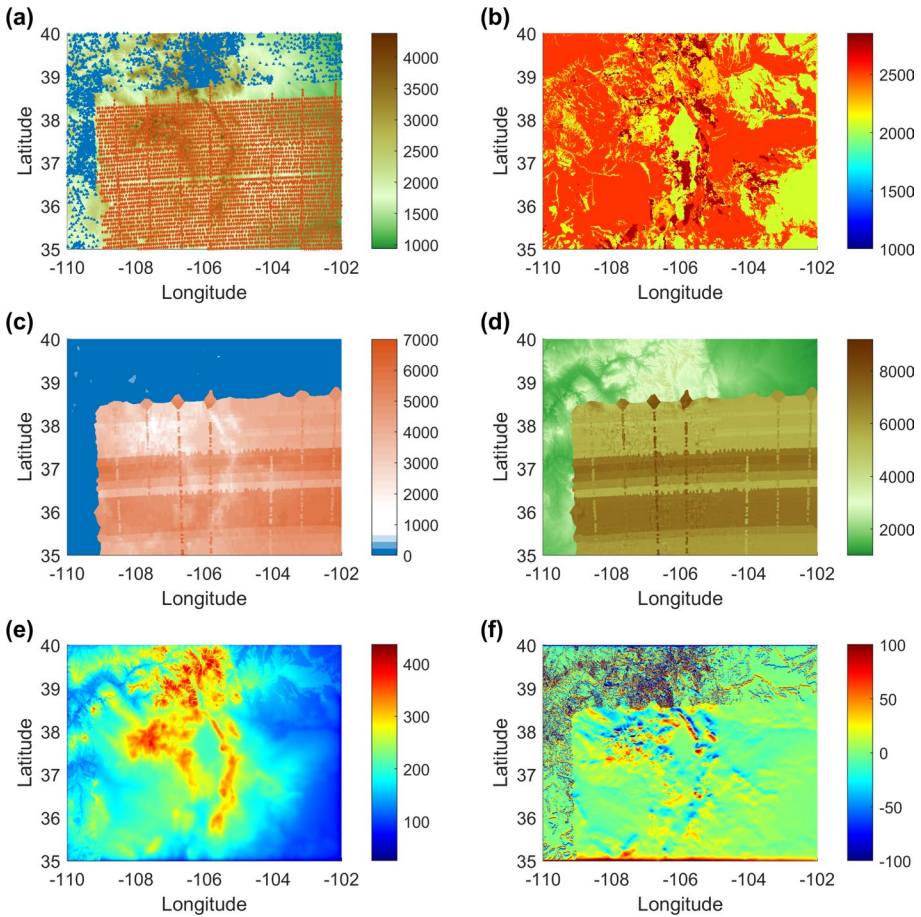
Fig. 10 **a** $3'' \times 3''$ resolution SRTM v4.1 DEM (Jarvis et al. 2008) of the Colorado test area and selected terrestrial (blue triangles) and airborne (red diamonds) gravity observation locations. **b** Laterally variable density distribution interpolated from the $30''$ resolution UNB_TopoDens model (Sheng et al. 2019). **c** Interpolated terrain clearance D. **d** The calculation surface $H_{cal} = h_{DEM} + D$. **e** CP-FFT calculated g_z component. **f** CP-FFT calculated T_{zz} component. Height values in meters, density in kg/m^3, g_z values in mGal, and T_{zz} in Eötvös

tvös, E_2 error below 0.1% for the T_{zz} component. Except for the T_{xx} and T_{yy} components, which exhibit slightly larger errors (MAE about 6 Eötvös), MAEs for other GGT components are generally below 1 Eötvös, which is sufficiently accurate for most practical applications. The space-domain solution takes more than 5 days computing values simply at the subset of 7991 observations, while the CP-FFT algorithm takes about 16 hours computing all 10 gravitational components on the size 9601×6001 computation grid (acceleration $\tau > 60000$), proving its capability for fast computation of gravitational signal induced by large DEM datasets on personal computers.
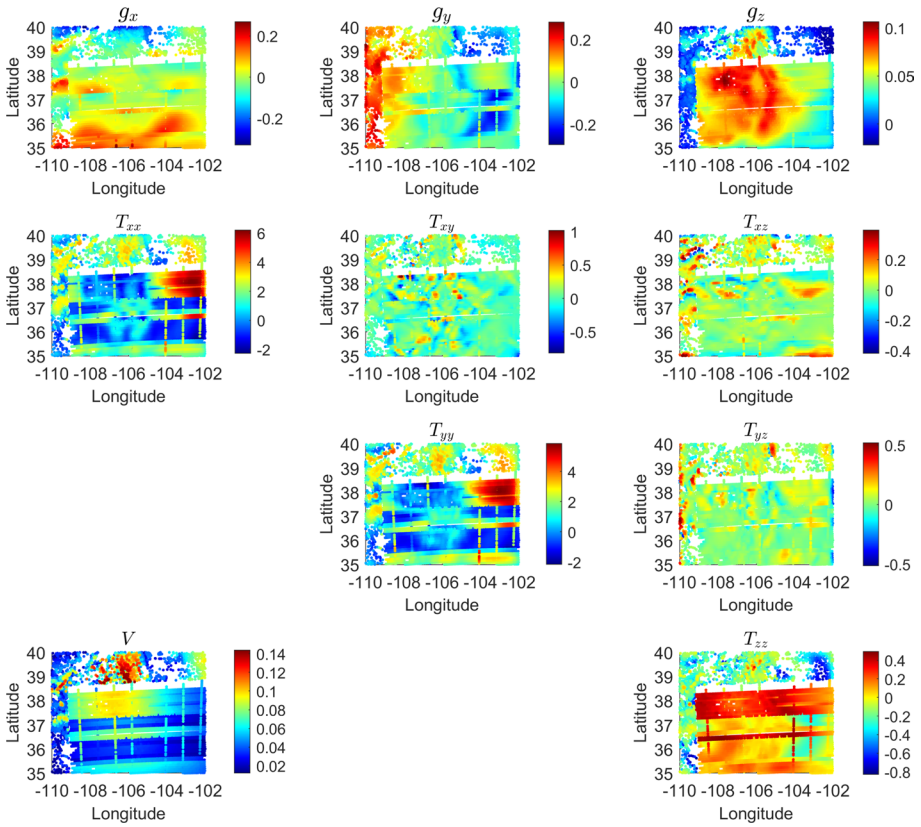
Fig. 11 Difference maps for GP, GV and GGT components between CP-FFT forward results and prism-summation computed reference values at the selected 7991 gravity observations in Fig. 10a. GP values in m²/s², GV values in mGal, GGT values in Eötvös

3.5 Magnetic Field Modeling

The final example is dedicated to the modeling of magnetic fields induced by a bathymetric model around 13°N on the Mid-Atlantic Ridge, where sea surface gravity, magnetic data, and near-seafloor magnetic fields have been measured and analyzed by several authors for the study of oceanic core complexes (OCC) (Mallows et al. 2012; Searle et al. 2019). As shown in Fig. 12, a patch of $0.5° \times 0.5°$ multibeam bathymetry data with $3'' \times 3''$ resolution is downloaded from NOAA's National Centers for Environmental Information (NCEI). To test our new algorithm for variable magnetization, we apply the inverted seafloor magnetization in Searle et al. (2019) in our forward modeling.

The computations are carried out both at the sea surface and at an undulating surface with 100 m constant height above the seafloor. The magnetic fields are induced from a 0.5 km thick source layer with either normally (positive magnetization) or reversely (negative magnetization) magnetized blocks. The magnetization is in the direction of a geocentric axial dipole with declination 0°, inclination 25.6° (Searle et al. 2019), and the background magnetic direction is calculated from the IGRF-13 model as declination −17°, inclination 21° (Alken et al. 2021).

Table 4 Statistics of the forward results of GP, GV and GGT components caused by the Colorado DEM model with laterally variable density (see Fig. 10) using CP-FFT and prism-summation algorithms. GP in m^2/s^2, GV in mGal, and GGT in Eötvös

Component	Quantity	Min	Max	Mean	RMS	E_2
V	Reference	318.278	803.929	617.015	626.621	0.010%
	CP-FFT	318.317	804.027	617.071	626.679	
	Difference	0.012	0.144	0.056	0.062	
g_x	Reference	−517.758	305.364	−13.327	111.505	0.077%
	CP-FFT	−518.023	305.565	−13.339	111.580	
	Difference	−0.330	0.269	−0.011	0.086	
g_y	Reference	−264.815	403.732	0.856	107.628	0.097%
	CP-FFT	−264.891	403.935	0.856	107.718	
	Difference	−0.295	0.283	−0.000	0.104	
g_z	Reference	43.584	432.737	211.587	224.841	0.022%
	CP-FFT	43.596	432.815	211.628	224.885	
	Difference	−0.022	0.107	0.041	0.050	
T_{xx}	Reference	−992.131	1119.208	−45.007	154.302	1.239%
	CP-FFT	−988.965	1120.782	−43.888	153.898	
	Difference	−2.274	6.201	1.119	1.912	
T_{xy}	Reference	−436.027	439.470	−0.890	58.078	0.268%
	CP-FFT	−436.375	439.478	−0.881	58.091	
	Difference	−0.814	1.015	0.009	0.156	
T_{xz}	Reference	−1167.491	482.814	1.662	70.753	0.123%
	CP-FFT	−1167.627	482.759	1.657	70.749	
	Difference	−0.417	0.395	−0.006	0.087	
T_{yy}	Reference	−1032.165	752.867	−38.061	148.047	1.277%
	CP-FFT	−1030.069	756.029	−36.882	147.669	
	Difference	−2.168	5.853	1.179	1.891	
T_{yz}	Reference	−1102.512	924.344	−16.851	79.078	0.118%
	CP-FFT	−1102.389	924.744	−16.840	79.081	
	Difference	−0.515	0.518	0.011	0.093	
T_{zz}	Reference	−1099.702	1462.005	83.068	272.108	0.096%
	CP-FFT	−1099.925	1461.328	82.997	272.020	
	Difference	−0.828	0.494	−0.071	0.261	

Using the prismatic solution as the precise reference, our CP-FFT algorithm ($N_L = N_H = N_h = 100$, $R_{FFT} = 2$ km, $N_{CP} = 50$) obtains MAEs below 1 nT, RMS errors below 0.2 nT, and E_2 errors below 0.3% for sea surface magnetic field modeling, and MAEs below 7 nT, RMS errors below 2 nT, and E_2 errors below 0.7% for all near-bottom magnetic vector components. More statistical details can be found in Table 5. The space-domain solution takes more than 2 days to complete the whole calculation (source grid size 601×601, computation grid size 591×591), while the CP-FFT algorithm costs only about 17 minutes (acceleration $\tau \approx 190$), proving its remarkable efficiency in computing magnetic components on both constant and undulating surfaces caused by densely-sampled, rough bathymetric models with variable magnetization.
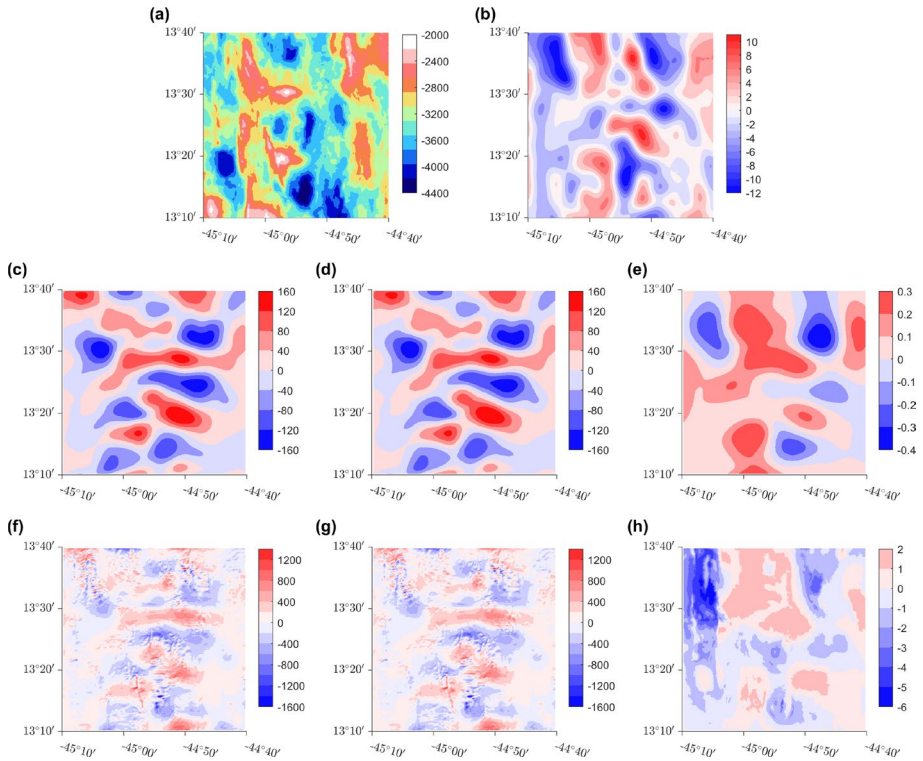
Fig. 12 Comparison of space-domain and CP-FFT forward results of sea surface and near-bottom magnetic fields induced by a bathymetric model with variable magnetization around 13°N on the Mid-Atlantic Ridge. **a** Bathymetry of the area. **b** Inverted seafloor magnetization digitized from Searle et al (2019, Fig. 5) c–e Sea surface magnetic anomaly B_e^{SS} calculated by using space-domain and CP-FFT algorithms and the corresponding difference. (f–h) Near-bottom magnetic anomaly B_e^{NB} calculated by using space-domain and CP-FFT algorithms and the corresponding difference. Bathymetry values in meters, magnetization in A/m, magnetic fields in nT

4 Conclusions

In this study, we have developed a new CP-FFT algorithm for fast and accurate computation of topographic gravitational and magnetic fields. We have made several improvements to the classical FFT-based terrain correction algorithm, including (a) CP decomposition instead of binomial expansion is applied to guarantee the convergence of the outer zone computation for rough terrain or bathymetry models, (b) the new method is extended to include GP, GV, GGT and magnetic field forward modeling on arbitrary undulating surfaces caused by topographic sources with variable density/magnetization, and (c) a GQML model is introduced to accelerate the computation of the inner zone effect. Numerical tests prove that our new algorithm has great advantage in computational speed over space-domain solutions while maintaining a sufficiently high accuracy well below existing instrumentation error levels.

Except for the sizes of the source and computation grids, computational efficiency of the new algorithm mainly depends on R_{FFT}, i.e., the radius separating the inner and outer computation zones. A larger separating radius would require more time-consuming

Table 5 Descriptive statistics of the forward results of magnetic effects of the bathymetric model in Fig. 12. SS stands for Sea Surface magnetic fields, and NB stands for Near Bottom magnetic fields. Units in nT

Component	Quantity	Min	Max	Mean	RMS	E_2
B_x^{SS}	Reference	−158.896	179.492	0.563	58.229	0.253%
	CP-FFT	−158.987	179.664	0.608	58.260	
	Difference	−0.425	0.373	0.044	0.147	
B_y^{SS}	Reference	−176.895	197.860	4.506	55.065	0.171%
	CP-FFT	−177.039	198.071	4.494	55.129	
	Difference	−0.312	0.224	−0.011	0.094	
B_z^{SS}	Reference	−247.406	237.712	−5.717	79.875	0.066%
	CP-FFT	−247.549	237.852	−5.722	79.920	
	Difference	−0.158	0.150	−0.005	0.052	
B_e^{SS}	Reference	−160.261	177.297	−2.776	56.947	0.250%
	CP-FFT	−160.453	177.505	−2.735	57.010	
	Difference	−0.419	0.363	0.041	0.142	
B_x^{NB}	Reference	−1469.905	1445.836	0.578	251.886	0.626%
	CP-FFT	−1468.329	1444.054	0.172	252.045	
	Difference	−6.218	3.008	−0.405	1.576	
B_y^{NB}	Reference	−1168.927	1238.702	1.729	233.707	0.316%
	CP-FFT	−1169.621	1240.074	1.639	233.897	
	Difference	−2.852	3.199	−0.090	0.740	
B_z^{NB}	Reference	−2250.195	1716.048	−8.209	321.703	0.050%
	CP-FFT	−2250.053	1715.736	−8.210	321.675	
	Difference	−1.172	0.762	−0.001	0.161	
B_e^{NB}	Reference	−1553.230	1394.238	−2.898	254.823	0.578%
	CP-FFT	−1554.978	1394.553	−3.236	254.968	
	Difference	−6.350	2.936	−0.338	1.473	

space-domain evaluation of inner-zone effects, while in the mean time accelerate the convergence of the outer-zone calculation. An empirical value of $R_{FFT} = \frac{\max(h) - \min(h)}{4}$, which equals to one fourth of the overall undulation of the input DEM, is recommended to better balance computational efficiency and accuracy. Besides, a value of $N_{CP} = 50$ for CP decomposition of the gravitational integration kernels is also recommended for the FFT-evaluated outer-zone effect to achieve sufficient accuracy with minimum computation amount. For the dimension of the CP decomposition, we recommend using $N_L = N_H = N_h = 100$ for computation areas at a scale of around 200×200 km, and $N_L = N_H = N_h = 200$ for computation areas at a scale of around 500×500 km. For calculation areas above 500 km, the influence of Earth curvature may become more significant, and the CP-FFT method may not be applicable.

The proposed method is developed in Cartesian coordinates, therefore, it should be used with caution when dealing with regional gravitational or magnetic modeling problems where planar approximation of the actual curved Earth can lead to significant errors. Extension of the method to include the curvature of the Earth through a resampling of the DEM may be possible. However, since most DEM products are provided on geographical grids, additional Cartesian-Spherical coordinate transformations and interpolations of both

the DEM and the calculated fields are required to obtain forward results also on geographical grids.

In our numerical tests, the inner zone effect is evaluated using prismatic solutions, with the topography represented by a step function. Using a more smooth polyhedral or bilinear representation of the topography for evaluation would certainly improve the accuracy of modeling. The computational cost will be slightly increased by choosing different height values for each mass line in our GQML model using triangular or bilinear interpolation within each grid cell. These may be treated in an updated version of our algorithm and computer code.

The new algorithm may be a ready substitute for existing methods. All source codes, including space-domain solutions, the CP-FFT algorithm, and several numerical examples, are released in MATLAB language. To our knowledge, there is no publicly available code that effectively and efficiently implements similar forward computing capabilities, which covers terrain-induced GP, GV, GGT and magnetic fields on arbitrary undulating surfaces, and takes into account variable density/magnetization distributions.

Appendix 1 CP-FFT Expressions for GP, GV, GGT with Horizontal Variable Density

Kernel functions for the gravitational potential (GP) V:

$$\mathcal{K}_V^{cb} = \int_h^0 \frac{1}{R} d\tilde{z} = I_1. \tag{22}$$

For the gravitational vector (GV) components g_x, g_y, g_z:

$$\mathcal{K}_{g_x}^{cb} = \frac{\partial}{\partial x}\left(\int_h^0 \frac{1}{R} d\tilde{z}\right) = (x - \tilde{x})I_2, \tag{23}$$

$$\mathcal{K}_{g_y}^{cb} = \frac{\partial}{\partial y}\left(\int_h^0 \frac{1}{R} d\tilde{z}\right) = (y - \tilde{y})I_2, \tag{24}$$

$$\mathcal{K}_{g_z}^{cb} = \frac{\partial}{\partial z}\left(\int_h^0 \frac{1}{R} d\tilde{z}\right) = J_1. \tag{25}$$

For the gravitational gradient tensor (GGT) components $T_{xx}, T_{xy}, T_{xz}, T_{yy}, T_{yz}, T_{zz}$:

$$\mathcal{K}_{T_{xx}}^{cb} = \frac{\partial^2}{\partial x^2}\left(\int_h^0 \frac{1}{R} d\tilde{z}\right) = 3(x - \tilde{x})^2 I_3 + I_2, \tag{26}$$

$$\mathcal{K}_{T_{xy}}^{cb} = \frac{\partial^2}{\partial x \partial y}\left(\int_h^0 \frac{1}{R} d\tilde{z}\right) = 3(x - \tilde{x})(y - \tilde{y})I_3, \tag{27}$$

$$\mathcal{K}_{T_{xz}}^{cb} = \frac{\partial^2}{\partial x \partial z}\left(\int_h^0 \frac{1}{R} d\tilde{z}\right) = (x - \tilde{x})J_3, \tag{28}$$

$$\mathcal{K}^{cb}_{T_{yy}} = \frac{\partial^2}{\partial y^2}\left(\int_h^0 \frac{1}{R}d\tilde{z}\right) = 3(y-\tilde{y})^2 I_3 + I_2, \tag{29}$$

$$\mathcal{K}^{cb}_{T_{yz}} = \frac{\partial^2}{\partial y \partial z}\left(\int_h^0 \frac{1}{R}d\tilde{z}\right) = (y-\tilde{y})J_3. \tag{30}$$

$$\mathcal{K}^{cb}_{T_{zz}} = \frac{\partial^2}{\partial z^2}\left(\int_h^0 \frac{1}{R}d\tilde{z}\right) = J_2. \tag{31}$$

Here

$$I_1 = \ln\frac{\sqrt{L^2+(H-h)^2}+(H-h)}{\sqrt{L^2+H^2}+H}, \tag{32}$$

$$I_2 = -\frac{1}{L^2}\left(\frac{H-h}{\sqrt{L^2+(H-h)^2}} - \frac{H}{\sqrt{L^2+H^2}}\right), \tag{33}$$

$$I_3 = -\frac{I_2}{L^2} - \frac{1}{3L^4}\left[\left(\frac{H-h}{\sqrt{L^2+(H-h)^2}}\right)^3 - \left(\frac{H}{\sqrt{L^2+H^2}}\right)^3\right], \tag{34}$$

$$J_1 = \frac{1}{\sqrt{L^2+(H-h)^2}} - \frac{1}{\sqrt{L^2+H^2}}, \tag{35}$$

$$J_2 = \frac{H}{[L^2+H^2]^{\frac{3}{2}}} - \frac{H-h}{[L^2+(H-h)^2]^{\frac{3}{2}}}, \tag{36}$$

$$J_3 = \frac{1}{[L^2+H^2]^{\frac{3}{2}}} - \frac{1}{[L^2+(H-h)^2]^{\frac{3}{2}}}. \tag{37}$$

The CP decompositions are applied to the functions I_i or J_i, $i = 1, 2, 3$, all of which are functions of (L, H, h). Extra factors $(x-\tilde{x})^i$ or $(y-\tilde{y})^i$, $i = 1, 2$ can be combined with $A_n(L)$ since both are functions of $(x-\tilde{x}, y-\tilde{y})$.

CP-FFT expression for the g_x component is:

$$\bar{g}^{cb}_x(x,y,H) \approx G\sum_{n=1}^{N_{CP}} \lambda_n B_n(H)\Big(\big[\rho(\tilde{x},\tilde{y})C_n(h)\big] * \big[(x-\tilde{x})A_n(L)\big]\Big), \tag{38}$$

with $A_n(L)$, $B_n(H)$ and $C_n(h)$ representing a CP decomposition of I_2.

CP-FFT expression for the T_{xx} component is:

$$\bar{T}_{xx}^{cb}(x,y,H) \approx G \sum_{n=1}^{N_{CP}} \lambda_n^{(1)} B_n^{(1)}(H)\Big(\big[\rho(\tilde{x},\tilde{y})C_n^{(1)}(h)\big] * \big[3(x-\tilde{x})^2 A_n^{(1)}(L)\big]\Big)$$

$$+G \sum_{n=1}^{N_{CP}} \lambda_n^{(2)} B_n^{(2)}(H)\Big(\big[\rho(\tilde{x},\tilde{y})C_n^{(2)}(h)\big] * A_n^{(2)}(L)\Big),$$

(39)

with $A_n^{(1)}(L)$, $B_n^{(1)}(H)$ and $C_n^{(1)}(h)$ representing a CP decomposition of I_3, and $A_n^{(2)}(L)$, $B_n^{(2)}(H)$ and $C_n^{(2)}(h)$ representing a CP decomposition of I_2.

The computation of the GGT components T_{xx} and T_{yy} requires the summation of two CP-FFTs, while all other components can be solved using one single CP decomposition.

Data Availability The MATLAB Tensor Toolbox Version 3.2.1 is hosted on GITLAB and is freely available at http://www.tensortoolbox.org. The Multibeam bathymetry data are downloaded from NOAA's National Centers for Environmental Information (NCEI). The SRTM v4.1 digital elevation datasets are freely available at http://dwtkns.com/srtm/. Data for the Colorado test area are available at https://geodesy.noaa.gov/GEOID/research/co-cm-experiment/. All data and source codes associated with this manuscript, including space-domain solutions, the CP-FFT algorithm, and several numerical examples, are licensed under MIT and published on Figshare repository Wu and Chen (2022).

References

Alken P, Thébault E, Beggan CD et al (2021) International geomagnetic reference field: the thirteenth generation. Earth Planets Space 73(1):49. https://doi.org/10.1186/s40623-020-01288-x

Asgharzadeh MF, von Frese RRB, Kim HR et al (2007) Spherical prism gravity effects by Gauss-Legendre quadrature integration. Geophys J Int 169(1):1–11. https://doi.org/10.1111/j.1365-246X.2007.03214.x

Balmino G (1994) Gravitational potential harmonics from the shape of an homogeneous body. Celest Mech Dyn Astronomy 60(3):331–364. https://doi.org/10.1007/BF00691901

Balmino G, Vales N, Bonvalot S et al (2012) Spherical harmonic modelling to ultra-high degree of bouguer and isostatic anomalies. J Geodesy 86(7):499–520. https://doi.org/10.1007/s00190-011-0533-4

Baykiev E, Ebbing J, Brönner M et al (2016) Forward modeling magnetic fields of induced and remanent magnetization in the lithosphere using tesseroids. Comput Geosci 96:124–135. https://doi.org/10.1016/j.cageo.2016.08.004 (www.sciencedirect.com/science/article/pii/S0098300416302278)

Benedek J, Papp G, Kalmar J (2018) Generalization techniques to reduce the number of volume elements for terrain effect calculations in fully analytical gravitational modelling. J Geodesy 92(4):361–381. https://doi.org/10.1007/s00190-017-1067-1

Bhattacharyya B (1964) Magnetic anomalies due to prism-shaped bodies with arbitrary polarization. Geophysics 29(4):517–531

Bouligand C, Glen JM, Blakely RJ (2014) Distribution of buried hydrothermal alteration deduced from high-resolution magnetic surveys in Yellowstone National Park. J Geophys Res Solid Earth 119(4):2013JB010-802. https://doi.org/10.1002/2013JB010802

Brett W. Bader TGK, et al (2021) Tensor Toolbox for MATLAB, Version 3.2.1. www.tensortoolbox.org

Bucha B, Janák J (2014) A MATLAB-based graphical user interface program for computing functionals of the geopotential up to ultra-high degrees and orders: efficient computation at irregular surfaces. Comput Geosci 66:219–227. https://doi.org/10.1016/j.cageo.2014.02.005

Bucha B, Kuhn M (2020) A numerical study on the integration radius separating convergent and divergent spherical harmonic series of topography-implied gravity. J Geodesy 94(12):112. https://doi.org/10.1007/s00190-020-01442-z

Bucha B, Sansò F (2021) Gravitational field modelling near irregularly shaped bodies using spherical harmonics: a case study for the asteroid (101955) Bennu. J Geodesy 95(5):56. https://doi.org/10.1007/s00190-021-01493-w

Bucha B, Hirt C, Kuhn M (2019) Cap integration in spectral gravity forward modelling up to the full gravity tensor. J Geodesy 93(9):1707–1737. https://doi.org/10.1007/s00190-019-01277-3

Bucha B, Hirt C, Kuhn M (2019) Divergence-free spherical harmonic gravity field modelling based on the Runge-Krarup theorem: a case study for the Moon. J Geodesy 93(4):489–513. https://doi.org/10.1007/s00190-018-1177-4

Cella F (2015) GTeC—a versatile MATLAB® tool for a detailed computation of the terrain correction and bouguer gravity anomalies. Comput Geosci 84:72–85. https://doi.org/10.1016/j.cageo.2015.07.015

Chen L, Liu L (2019) Fast and accurate forward modelling of gravity field using prismatic grids. Geophys J Int 216(2):1062–1071. https://doi.org/10.1093/gji/ggy480

Claessens SJ, Hirt C (2013) Ellipsoidal topographic potential: new solutions for spectral forward gravity modeling of topography with respect to a reference ellipsoid. J Geophys Res Solid Earth 118(11):5991–6002. https://doi.org/10.1002/2013JB010457

Costin O, Costin RD, Ogle C et al (2022) On the domain of convergence of spherical harmonic expansions. Commun Math Phys 389(2):875–897. https://doi.org/10.1007/s00220-021-04262-0

Deng XL, Shen WB (2018) Evaluation of optimal formulas for gravitational tensors up to gravitational curvatures of a tesseroid. Surv Geophys 39(3):365–399. https://doi.org/10.1007/s10712-018-9460-8

Du J, Chen C, Lesur V et al (2015) Magnetic potential, vector and gradient tensor fields of a tesseroid in a geocentric spherical coordinate system. Geophys J Int 201(3):1977–2007. https://doi.org/10.1093/gji/ggv123

D'Urso MG, Trotta S (2017) Gravity anomaly of polyhedral bodies having a polynomial density contrast. Surv Geophys 38(4):781–832. https://doi.org/10.1007/s10712-017-9411-9

Featherstone WE, Hirt C, Kuhn M (2013) Band-limited Bouguer gravity identifies new basins on the Moon. J Geophys Res Planets 118(6):1397–1413. https://doi.org/10.1002/jgre.20101. (**agupubs.onlinelibrary.wiley.com/doi/abs/10.1002/jgre.20101**)

Forsberg R (1984) Study of terrain reductions, density anomalies and geo-physical inversion methods in gravity field modelling. Tech. rep., Report 355, Department of Geodetic Science and Surveying. The Ohio State University, Columbus, USA

Forsberg R (1985) Gravity field terrain effect computations by FFT. Bull Geodesique 59(4):342–360

Fukushima T (2018) Accurate computation of gravitational field of a tesseroid. J Geodesy 92(12):1371–1386. https://doi.org/10.1007/s00190-018-1126-2

Fukushima T (2020) Speed and accuracy improvements in standard algorithm for prismatic gravitational field. Geophys J Int 222(3):1898–1908. https://doi.org/10.1093/gji/ggaa240

Garcia-Abdeslem J (2005) The gravitational attraction of a right rectangular prism with density varying with depth following a cubic polynomial. Geophysics 70(6):J39–J42. https://doi.org/10.1190/1.2122413

Garmier R, Barriot JP, Konopliv AS et al (2002) Modeling of the eros gravity field as an ellipsoidal harmonic expansion from the near doppler tracking data. Geophys Res Lett 29(8):1231. https://doi.org/10.1029/2001GL013768

Goyal R, Featherstone WE, Tsoulis D et al (2020) Efficient spatial-spectral computation of local planar gravimetric terrain corrections from high-resolution digital elevation models. Geophysl J Int 221(3):1820–1831. https://doi.org/10.1093/gji/ggaa107. arxiv.org/abs/academic.oup.com/gji/article-pdf/221/3/1820/33209916/ggaa107.pdf

Grauch VJS (1987) A new variable-magnetization terrain correction method for aeromagnetic data. Geophysics 52(1):94–107. https://doi.org/10.1190/1.1442244

Grombein T, Seitz K, Heck B (2016) The Rock-Water-Ice topographic gravity field model RWI_TOPO_2015 and its comparison to a conventional rock-equivalent version. Surv Geophys 37(5):937–976. https://doi.org/10.1007/s10712-016-9376-0

Górski KM, Bills BG, Konopliv AS (2018) A high resolution Mars surface gravity grid. Planet Space Sci 160:84–106. https://doi.org/10.1016/j.pss.2018.03.015 (www.sciencedirect.com/science/article/pii/S0032063317304658)

Hartmann J, Moosdorf N (2012) The new global lithological map database GLiM: a representation of rock properties at the Earth surface. Geochem Geophys Geosyst 13(12). https://doi.org/ https://doi.org/10.1029/2012GC004370, URL https://agupubs.onlinelibrary.wiley.com/doi/ abs/10.1029/2012GC004370

Heck B, Seitz K (2007) A comparison of the tesseroid, prism and point-mass approaches for mass reductions in gravity field modelling. J Geodesy 81(2):121–136. https://doi.org/10.1007/s00190-006-0094-0

Hildenbrand TG, Rosenbaum JG, Kauahikaua JP (1993) Aeromagnetic study of the Island of Hawaii. J Geophys Res Solid Earth 98(B3):4099–4119. https://doi.org/10.1029/92JB02483. (**agupubs.onlinelibrary.wiley.com/doi/abs/10.1029/92JB02483**)

Hirt C (2012) Efficient and accurate high-degree spherical harmonic synthesis of gravity field functionals at the Earth's surface using the gradient approach. J Geodesy 86(9):729–744. https://doi.org/10.1007/ s00190-012-0550-y

Hirt C, Kuhn M (2014) Band-limited topographic mass distribution generates full-spectrum gravity field: gravity forward modeling in the spectral and spatial domains revisited. J Geophys Res Solid Earth 119(4):3646–3661. https://doi.org/10.1002/2013JB010900

Hirt C, Kuhn M (2017) Convergence and divergence in spherical harmonic series of the gravitational field generated by high-resolution planetary topography-A case study for the Moon. J Geophys Res Planets 122(8):1727–1746. https://doi.org/10.1002/2017JE005298. (**agupubs.onlinelibrary.wiley.com/doi/ abs/10.1002/2017JE005298**)

Hirt C, Rexer M (2015) Earth 2014: 1 arc-min shape, topography, bedrock and ice-sheet models-available as gridded data and degree-10,800 spherical harmonics. Int J Appl Earth Observ Geoinf 39:103–112. https://doi.org/10.1016/j.jag.2015.03.001 (www.sciencedirect.com/science/article/pii/S030324341 5000513)

Hirt C, Claessens S, Fecher T et al (2013) New ultrahigh-resolution picture of Earth's gravity field. Geophys Res Lett 40(16):4279–4283. https://doi.org/10.1002/grl.50838

Hirt C, Yang M, Kuhn M et al (2019) SRTM2gravity: an ultrahigh resolution global model of gravimetric terrain corrections. Geophys Res Lett 46(9):4618–4627. https://doi.org/10.1029/2019GL082521. (**agupubs.onlinelibrary.wiley.com/doi/abs/10.1029/2019GL082521**)

Hogue JD, Renaut RA, Vatankhah S (2020) A tutorial and open source software for the efficient evaluation of gravity and magnetic kernels. Comput Geosci 144(104):575. https://doi.org/10.1016/j.cageo.2020. 104575

Holstein H (2003) Gravimagnetic anomaly formulas for polyhedra of spatially linear media. Geophysics 68(1):157–167. https://doi.org/10.1190/1.1543203

Holzrichter N, Szwillus W, Gotze HJ (2019) An adaptive topography correction method of gravity field and gradient measurements by polyhedral bodies. Geophys J Int 218(2):1057–1070. https://doi.org/ 10.1093/gji/ggz211

Hu X, Jekeli C (2015) A numerical comparison of spherical, spheroidal and ellipsoidal harmonic gravitational field models for small non-spherical bodies: examples for the Martian moons. J Geodesy 89(2):159–177. https://doi.org/10.1007/s00190-014-0769-x

Ince ES, Barthelmes F, Reissland S et al (2019) ICGEM-15 years of successful collection and distribution of global gravitational models, associated services, and future plans. Earth Syst Sci Data 11(2):647–674. https://doi.org/10.5194/essd-11-647-2019

Ince ES, Abrykosov O, Foerste C et al (2020) Forward gravity modelling to augment high-resolution combined gravity field models. Surv Geophys 41(4):767–804. https://doi.org/10.1007/ s10712-020-09590-9

Jarvis A, Reuter HI, Nelson A, et al (2008) Hole-filled SRTM for the globe Version 4, available from the CGIAR-CSI SRTM 90m Database. http://srtm.csi.cgiar.org

Jekeli C, Zhu LZ (2006) Comparison of methods to model the gravitational gradients from topographic data bases. Geophys J Int 166(3):999–1014. https://doi.org/10.1111/j.1365-246X.2006.03063.x

Jiang L, Liu J, Zhang J et al (2018) Analytic expressions for the gravity gradient tensor of 3D prisms with depth-dependent density. Surv Geophys 39(3):337–363. https://doi.org/10.1007/s10712-017-9455-x

Karcol R (2018) The gravitational potential and its derivatives of a right rectangular prism with depth-dependent density following an n-th degree polynomial. Studia Geophysica et Geodaetica 62(3):427–449. https://doi.org/10.1007/s11200-017-0365-7

Kolda TG, Bader BW (2009) Tensor decompositions and applications. SIAM Rev 51(3):455–500. https:// doi.org/10.1137/07070111X

Li YC, Sideris MG (1994) Improved gravimetric terrain corrections. Geophys J Int 119(3):740–752. https:// doi.org/10.1111/j.1365-246X.1994.tb04013.x

Lin M, Denker H, Muller J (2020) Gravity field modeling using tesseroids with variable density in the vertical direction. Surv Geophys 41(4):723–765. https://doi.org/10.1007/s10712-020-09585-6

Liu S, Fedi M, Hu X et al (2018) Extracting induced and premanent magnetizations from magnetic data modeling. J Geophys Res Solid Earth 123(11):9290–9309. https://doi.org/10.1029/2017JB015364. (agupubs.onlinelibrary.wiley.com/doi/abs/10.1029/2017JB015364)

Macdonald KC, Miller SP, Luyendyk BP et al (1983) Investigation of a Vine-Matthews Magnetic Lineation from a submersible: the source and character of marine magnetic anomalies. J Geophys Res Solid Earth 88(B4):3403–3418. https://doi.org/10.1029/JB088iB04p03403

Mallows C, Searle RC (2012) A geophysical study of oceanic core complexes and surrounding terrain, Mid-Atlantic Ridge 13°N-14°N. Geochem Geophys Geosyst 13(6). https://doi.org/ https://doi.org/10.1029/2012GC004075, URL https://agupubs.onlinelibrary.wiley.com/doi/ abs/10.1029/2012GC004075

Martinec Z, Pec K, Bursa M (1989) The Phobos gravitational field modeled on the basis of its topography. Earth Moon Planets 45(3):219–235. https://doi.org/10.1007/BF00057745

Martinec Z, Vaníček P, Mainville A et al (1996) Evaluation of topographical effects in precise geoid computation from densely sampled heights. J Geodesy 70(11):746–754. https://doi.org/10.1007/ BF00867153

Moorkamp M, Jegen M, Roberts A et al (2010) Massively parallel forward modeling of scalar and tensor gravimetry data. Comput Geosci 36(5):680–686. https://doi.org/10.1016/j.cageo.2009.09.018 (www.sciencedirect.com/science/article/pii/S0098300410000579)

Nagy D, Papp G, Benedek J (2000) The gravitational potential and its derivatives for the prism. J Geodesy 74(7–8):552–560

Parker RL (1973) The rapid calculation of potential anomalies. Geophys J Royal Astron Soc 31(4):447–455

Parker RL (1996) Improved fourier terrain correction 2. Geophysics 61(2):365–372. https://doi.org/10. 1190/1.1443965

Parker RL, Huestis SP (1974) The inversion of magnetic anomalies in the presence of topography. J Geophys Res 79(11):1587–1593. https://doi.org/10.1029/JB079i011p01587

Pavlis NK, Holmes SA, Kenyon SC et al (2012) The development and evaluation of the Earth Gravitational Model 2008 (EGM2008). J Geophys Res Solid Earth 117(B04):406. https://doi.org/10.1029/ 2011JB008916

Pedersen LB, Bastani M, Kamm J (2015) Gravity gradient and magnetic terrain effects for airborne applications-a practical fast Fourier transform technique. Geophysics 80(2):J19–J26. https://doi. org/10.1190/GEO2014-0083.1

Plouff D (1976) Gravity and magnetic fields of polygonal prisms and application to magnetic terrain corrections. Geophysics 41(4):727–741

Ramillien G (2002) Gravity/magnetic potential of uneven shell topography. J Geodesy 76(3):139–149. https://doi.org/10.1007/s00190-002-0193-5

Reimond S, Baur O (2016) Spheroidal and ellipsoidal harmonic expansions of the gravitational potential of small solar system bodies. case study: Comet 67P/Churyumov-Gerasimenko. J Geophys Res Planets 121(3):497–515. https://doi.org/10.1002/2015JE004965

Ren Z, Zhong Y, Chen C et al (2018) Gravity gradient tensor of arbitrary 3D polyhedral bodies with up to third-order polynomial horizontal and vertical mass contrasts. Surv Geophys 39(5):901–935. https://doi.org/10.1007/s10712-018-9467-1

Rexer M (2017) Spectral solutions to the topographic potential in the context of high-resolution global gravity field modelling. PhD thesis, Technische Universität München, München, Germany

Rexer M, Hirt C, Claessens S et al (2016) Layer-based modelling of the Earth's gravitational potential up to 10-km scale in spherical harmonics in spherical and ellipsoidal approximation. Surv Geophys 37(6):1035–1074. https://doi.org/10.1007/s10712-016-9382-2

Roussel C, Verdun J, Cali J et al (2015) Complete gravity field of an ellipsoidal prism by gauss-legendre quadrature. Geophys J Int 203(3):2220–2236

Rummel R, Rapp RH, Sunkel H, et al (1988) Comparisons of global topographic-isostatic models to the Earth's observed gravity field. Tech. rep., Rep. No. 388, Dpt. of Geodetic Sci. and Surv., Ohio State University, Columbus, Ohio

Sanso FF, Sideris MG (2013) Geoid determination: theory and methods. Lecture notes in Earth system sciences, Springer, Berlin

Saraswati AT, Cattin R, Mazzotti S et al (2019) New analytical solution and associated software for computing full-tensor gravitational field due to irregularly shaped bodies. J Geodesy 93(12):2481–2497. https://doi.org/10.1007/s00190-019-01309-y

Searle RC, MacLeod CJ, Peirce C et al (2019) The Mid-Atlantic Ridge near 13°20′N: high-resolution magnetic and bathymetry imaging. Geochem Geophys Geosyst 20(1):295–313. https://doi.org/10. 1029/2018GC007940. (agupubs.onlinelibrary.wiley.com/doi/abs/10.1029/2018GC007940)

Sheng MB, Shaw C, Vaníček P et al (2019) Formulation and validation of a global laterally varying topographical density model. Tectonophysics 762:45–60. https://doi.org/10.1016/j.tecto.2019.04.005 (www.sciencedirect.com/science/article/pii/S0040195119301155)

Sideris MG (1984) Computation of gravimetric terrain corrections using fast Fourier transform techniques. Master's thesis, University of Calgary, Calgary, AB. https://doi.org/10.11575/PRISM/14395

Sprlak M, Han SC (2021) On the use of spherical harmonic series inside the minimum Brillouin sphere: theoretical review and evaluation by GRAIL and LOLA satellite data. Earth Sci Rev 222(103):739. https://doi.org/10.1016/j.earscirev.2021.103739 (www.sciencedirect.com/science/article/pii/S0012825221002403)

Sprlak M, Han SC, Featherstone WE (2018) Forward modelling of global gravity fields with 3D density structures and an application to the high-resolution (2 km) gravity fields of the Moon. J Geodesy 92(8):847–862. https://doi.org/10.1007/s00190-017-1098-7

Sprlak M, Han SC, Featherstone WE (2020) Spheroidal forward modelling of the gravitational fields of 1 Ceres and the Moon. Icarus 335(113):412. https://doi.org/10.1016/j.icarus.2019.113412 (www.sciencedirect.com/science/article/pii/S0019103519303252)

Tenzer R, Chen W, Tsoulis D et al (2015) Analysis of the refined CRUST1.0 crustal model and its gravity field. Surv Geophys 36(1):139–165. https://doi.org/10.1007/s10712-014-9299-6

Tontini FC, Cocchi L, Carmisciano C (2008) Potential-field inversion for a layer with uneven thickness: the Tyrrhenian Sea density model. Phys Earth Planet Interiors 166(1–2):105–111. https://doi.org/10.1016/j.pepi.2007.10.007

Tontini FC, Cocchi L, Carmisciano C (2009) Rapid 3-D forward model of potential fields with application to the Palinuro Seamount magnetic anomaly (southern Tyrrhenian Sea, Italy). J Geophys Res Solid Earth 114(B02):103. https://doi.org/10.1029/2008JB005907

Tsoulis D (2001) Terrain correction computations for a densely sampled DTM in the Bavarian Alps. J Geodesy 75(5–6):291–307. https://doi.org/10.1007/s001900100176

Tsoulis D (2012) Analytical computation of the full gravity tensor of a homogeneous arbitrarily shaped polyhedral source using line integrals. Geophysics 77(2):F1–F11. https://doi.org/10.1190/GEO2010-0334.1

Tsoulis D, Novak P, Kadlec M (2009) Evaluation of precise terrain effects using high-resolution digital elevation models. J Geophys Res Solid Earth 114(B02):404. https://doi.org/10.1029/2008JB005639

Uieda L, Barbosa VCF, Braitenberg C (2016) Tesseroids: forward-modeling gravitational fields in spherical coordinates. Geophysics 81(5):F41–F48

Vatankhah S, Liu S, Renaut RA et al (2022) An efficient alternating algorithm for the L-p-norm cross-gradient joint inversion of gravity and magnetic data using the 2-D Fast Fourier Transform. IEEE Trans Geosci Remote Sens 60(4500):416. https://doi.org/10.1109/TGRS.2020.3033043

Vogel CR (2002) Computational methods for inverse problems, vol 23. SIAM

Wang YM, Yang X (2013) On the spherical and spheroidal harmonic expansion of the gravitational potential of the topographic masses. J Geodesy 87(10):909–921. https://doi.org/10.1007/s00190-013-0654-z

Wang YM, Sánchez L, Ågren J et al (2021) Colorado geoid computation experiment: overview and summary. J Geodesy 95(12):127. https://doi.org/10.1007/s00190-021-01567-9

Werner RA, Scheeres DJ (1997) Exterior gravitation of a polyhedron derived and compared with harmonic and mascon gravitation representations of asteroid 4769 Castalia. Celest Mech Dyn Astro 65(3):313–344. https://doi.org/10.1007/BF00053511

Wieczorek M (2015) 10.05 - gravity and topography of the terrestrial planets. In: Schubert G (ed) Treatise on Geophysics (Second Edition), second edition edn. Elsevier, Oxford, p 153 – 193, https://doi.org/10.1016/B978-0-444-53802-4.00169-X, http://www.sciencedirect.com/science/article/pii/B9780444453802400169X

Wieczorek MA, Phillips RJ (1998) Potential anomalies on a sphere: applications to the thickness of the lunar crust. J Geophys Res Planets 103(E1):1715–1724. https://doi.org/10.1029/97JE03136

Wild-Pfeiffer F (2008) A comparison of different mass elements for use in gravity gradiometry. J Geodesy 82(10):637–653. https://doi.org/10.1007/s00190-008-0219-8

Wu L (2016) Efficient modelling of gravity effects due to topographic masses using the Gauss-FFT method. Geophys J Int 205(1):160–178. https://doi.org/10.1093/gji/ggw010

Wu L (2018) Efficient modeling of gravity fields caused by sources with arbitrary geometry and arbitrary density distribution. Surv Geophys 39(3):401–434. https://doi.org/10.1007/s10712-018-9461-7

Wu L (2021) Modified Parker's method for gravitational forward and inverse modeling using general polyhedral models. J Geophys Res Solid Earth 126(10):e2021JB022-553. https://doi.org/10.1029/2021JB022553

Wu L, Chen L (2022) Data and code for "fast computation of terrain-induced gravitational and magnetic effects on arbitrary undulating surfaces". https://doi.org/10.6084/m9.figshare.18515936.v4, https://

figshare.com/articles/software/Fast_computation_of_terrain-induced_gravitational_and_magnetic_effects_on_arbitrary_undulating_surfaces/18515936

Wu L, Tian G (2014) High-precision Fourier forward modeling of potential fields. Geophysics 79(5):G59–G68. https://doi.org/10.1190/GEO2014-0039.1

Yang M, Hirt C, Pail R (2020) TGF: a new MATLAB-based software for terrain-related gravity field calculations. Remote Sens 12(7):1063 (https://www.mdpi.com/2072-4292/12/7/1063)

Zhang S, Meng X, Chen Z et al (2015) Rapid calculation of gravity anomalies based on residual node densities and its GPU implementation. Comput Geosci 83:139–145. https://doi.org/10.1016/j.cageo.2015.06.022

Zhang Y, Chen C (2018) Forward calculation of gravity and its gradient using polyhedral representation of density interfaces: an application of spherical or ellipsoidal topographic gravity effect. J Geodesy 92(2):205–218. https://doi.org/10.1007/s00190-017-1057-3

Zhang Y, Wong YS (2015) BTTB-based numerical schemes for three-dimensional gravity field inversion. Geophys J Int 203(1):243–256. https://doi.org/10.1093/gji/ggv301

Zhao G, Chen B, Chen L et al (2018) High-accuracy 3D Fourier forward modeling of gravity field based on the Gauss-FFT technique. J Appl Geophys 150:294–303 (http://www.sciencedirect.com/science/article/pii/S0926985117301751)

Zingerle P, Pail R, Gruber T et al (2020) The combined global gravity field model XGM2019e. J Geodesy 94(7):66. https://doi.org/10.1007/s00190-020-01398-0

Authors and Affiliations

Leyuan Wu[1] · Longwei Chen[2]

Leyuan Wu
leyuanwu@zjut.edu.cn

[1]   Key Laboratory of Quantum Precision Measurement of Zhejiang Province, Center for Optics and Optoelectronics Research (COOR), Collaborative Innovation Center for Information Technology in Biological and Medical Physics, College of Science, Zhejiang University of Technology, Liuhe Road, Hangzhou 310023, Zhejiang, China

[2]   Guangxi Key Laboratory of Exploration For Hidden Metallic Ore Deposits, College of Earth Sciences, Guilin University of Technology, Yanshan, Guilin 541006, Guangxi, China